Centrum voor Wiskunde en Informatica

REPORT*RAPPORT*

MAS

Modelling, Analysis and Simulation

Modelling, Analysis and Simulation

Five-Equation Model for Compressible Two-Fluid Flow

J. Wackers, B. Koren

REPORT MAS-E0414 AUGUST 2004

CWI is the National Research Institute for Mathematics and Computer Science. It is sponsored by the Netherlands Organization for Scientific Research (NWO).
CWI is a founding member of ERCIM, the European Research Consortium for Informatics and Mathematics.

CWI's research has a theme-oriented structure and is grouped into four clusters. Listed below are the names of the clusters and in parentheses their acronyms.

Probability, Networks and Algorithms (PNA)

Software Engineering (SEN)

Modelling, Analysis and Simulation (MAS)

Information Systems (INS)

P.O. Box 94079, 1090 GB Amsterdam (NL)
Kruislaan 413, 1098 SJ Amsterdam (NL)
Telephone +31 20 592 9333
Telefax +31 20 592 4199

ISSN 1386-3703

Five-Equation Model for Compressible Two-Fluid Flow

ABSTRACT
An interface-capturing, five-equation model for compressible two-fluid flow is presented, that is based on a consistent, physical model for the flow in the numerical transition layer. The flow model is conservative and pressure-oscillation free. Due to the absence of an interface model in the capturing technique, the implementation of the model in existing flow solvers is very simple. The flow equations are the bulk-fluid equations, combined with mass and energy equations for one of the two fluids. The latter equation contains a source term, to account for the energy exchange between the fluids. The physical flow model enables the derivation of an exact expression for this source term, both in continuous and in discontinuous flow. The system is solved numerically with a limited second-order accurate finite-volume technique. Linde's HLL Riemann solver is used. This solver is simplified here and its combination with the second-order scheme is studied. When the solver is adapted to two-fluid flow, the source term in the flow equations is incorporated in the Riemann solver. Further, the total source term in the cells is integrated over each cell. Numerical tests are performed on 1D shock-tube problems and on 2D shock-bubble interactions. The results confirm that the method is pressure-oscillation free and show that shocks are captured sharply. Good agreement with known solutions is obtained. Two appendices show an approximate model for shocks in physical two-phase media and a theoretical study of the interaction of shocks with plane interfaces, which is used to analyse the shock-bubble interactions.

2000 Mathematics Subject Classification: 65M20, 65M60, 76J20, 76M12, 76N15
Keywords and Phrases: compressible two-fluid flow; interface capturing; conservation; energy exchange; source term; HLL Riemann solver; second-order accurate finite-volume discretisation
Note: This research was supported by the Dutch government through the national program BSIK: knowledge and research capacity, in the ICT project BRICKS (http://www.bsik-bricks.nl), theme MSV1, and was carried out under CWI project MAS2.1 `Computational Fluid Dynamics and Computational Electromagnetics'.

Five-Equation Model for Compressible Two-Fluid Flow

Jeroen Wackers, Barry Koren
CWI
P.O. Box 94079, 1090 GB Amsterdam, The Netherlands

ABSTRACT

An interface-capturing, five-equation model for compressible two-fluid flow is presented, that is based on a consistent, physical model for the flow in the numerical transition layer. The flow model is conservative and pressure-oscillation free. Due to the absence of an interface model in the capturing technique, the implementation of the model in existing flow solvers is very simple.

The flow equations are the bulk-fluid equations, combined with mass and energy equations for one of the two fluids. The latter equation contains a source term, to account for the energy exchange between the fluids. The physical flow model enables the derivation of an exact expression for this source term, both in continuous and in discontinuous flow.

The system is solved numerically with a limited second-order accurate finite-volume technique. Linde's HLL Riemann solver is used. This solver is simplified here and its combination with the second-order scheme is studied. When the solver is adapted to two-fluid flow, the source term in the flow equations is incorporated in the Riemann solver. Further, the total source term in the cells is integrated over each cell.

Numerical tests are performed on 1D shock-tube problems and on 2D shock-bubble interactions. The results confirm that the method is pressure-oscillation free and show that shocks are captured sharply. Good agreement with known solutions is obtained.

Two appendices show an approximate model for shocks in physical two-phase media and a theoretical study of the interaction of shocks with plane interfaces, which is used to analyse the shock-bubble interactions.

2000 Mathematics Subject Classification: 65M20, 65M60, 76J20, 76M12, 76N15
Keywords and Phrases: compressible two-fluid flow, interface capturing, conservation, energy exchange, source term, HLL Riemann solver, second-order accurate finite-volume discretisation.
Note: This research was supported by the Dutch government through the national program BSIK: knowledge and research capacity, in the ICT project BRICKS (http://www.bsik-bricks.nl), theme MSV1, and was carried out under CWI project MAS2.1 'Computational Fluid Dynamics and Computational Electromagnetics'.

Table of Contents

Chapter 1
Introduction

Two-fluid flow problems appear in many applications in physics and engineering. In these problems, the flow medium consists of two or more fluids, which do not mix. Instead, a sharp interface separates the pure fluids. A challenge in the numerical simulation of these flows is that a model for the interface must be coupled with a fluid-flow model. If these models do not fit together, then the flow solution may contain large errors.

One class of two-fluid models is known as interface-capturing techniques. These methods do not use an explicit interface model. Instead, the fluid is modeled as a mixture of the pure fluids everywhere, where away from the interface, the 'mixture' contains only one component. The interface itself appears as a smooth, numerically smeared transition from one fluid to the other. Thus, no special model is needed for the behaviour of the flow in the interface cells and the interface motion follows implicitly from the flow solution.

These models have two advantages over interface-tracking methods as the volume-of-fluid [13] and level-set [22, 28] techniques, that do have an explicit interface model. First, there is no need to implement an (often complex) algorithm for the interface motion, the capturing flow equations are basically equivalent to single-fluid flow equations. Therefore, capturing models can be implemented in existing flow solvers very easily. And secondly, tracking methods are ill-suited for conservative computation of compressible flows. The interface-motion models are usually based on a convection equation, that does not necessarily fit in with the conservation laws on which the flow model is based. Thus, rigorous enforcement of conservation, but with the interface in an improper location relative to the flow variables, leads to large local errors in, especially, the pressure. Therefore, most compressible interface-tracking techniques, like the successful ghost-fluid method [9], are locally non-conservative [8, 17]. This is a disadvantage for solving problems with strong shocks.

A conservative formulation is possible for compressible capturing models, but it depends on a proper model for the numerical mixture. Many capturing models use the single-fluid flow equations together with one extra transport equation for a parameter that determines the properties of the mixture, like the mass fraction of one of the fluids. Abgrall and Karni [2] have shown that conservative formulations of these models lead to pressure oscillations, i.e. pressure errors near the two-fluid interface that do not decrease on grid refinement. Therefore, some capturing techniques have been developed that also, locally, abandon conservation [1, 15].

Another possibility is to base the numerical mixture model on the equations for two-phase flow, that describe the behaviour of physical mixtures. These models use separate pressures, velocities and densities for each of the fluids. Some researchers solve these equations directly [3, 26]. Another popular approach, introduced by Kapila et al. [14] and extended in, e.g., [10], is to simplify the two-phase model, by taking a limit, to a form that is suitable for numerical mixtures. A model with comparable properties is suggested by Ton [30]. Unfortunately, these models need an approximate closure for a non-conservative term, that appears when a shock hits a two-fluid interface.

In this report, a conservative capturing method is presented, which is an extension of the method that Van Brummelen and Koren [6] introduced for barotropic flows. The method is based on a consistent physical model for the numerical mixture itself and all flow equations are derived directly from this mixture model. The result is a method which is similar to the Kapila model, but the physical mixture model makes it possible to derive an exact closure for the flow equations, in the case when a shock hits the interface. The method is therefore fully conservative.

The current two-fluid flow model is combined with a second-order accurate finite-volume discretisation and an adaptation of Linde's HLL approximate Riemann solver [19]. The result is a simple and efficient numerical method, which can be easily implemented in any existing single-fluid flow solver.

The report starts with a description of the mixture model and the derivation of the flow equations, in chapter 2. Chapter 3 analyses the source term, which appears in the flow equations, and derives the closure of the system for discontinuous flow. The numerical method is described, with a discussion of an improved version of Linde's HLL solver in chapter 4 and the adaptation of this solver to two-fluid flow in chapter 5. The performance of the method is tested on 1D and 2D problems in chapter 6.

The report contains two appendices. Appendix I describes an approximate mixture-shock model for strong shocks, which was obtained during the development of the five-equation model, although it is not connected with that model. Appendix II contains an analysis of the interaction of shocks with plane two-fluid interfaces. The results are generally applicable, they are applied here to the 2D test problems from chapter 6.

Chapter 2
Flow equations

This chapter describes the physical laws underlying the flow model. A physical model for compressible two-fluid flow without friction and heat conduction is developed and differential equations plus additional algebraic relations, that are consistent with this physical model, are derived.

2.1. PHYSICAL MODEL FOR TWO-FLUID FLOW

The physical model used here for two-fluid flow is based on a two-phase flow model, in which the entire flow domain is filled with a mixture of the two fluids. However, in this underlying two-phase model, the fluids are not mixed on the molecular level: the 'mixture' consists of very small elements of the two pure fluids, arranged in an irregular pattern. So the fluid is a mixture in the macroscopic sense, but on a microscopic level the two fluids keep their own pure-fluid behaviour. Each flow element has its own density, velocity and pressure and the elements interact by exerting forces on each other, thus exchanging work, and by exchanging heat.

For our (simpler) two-fluid model, some aspects of the above two-phase model are kept. Most importantly, we still assume that *both* fluids are present *everywhere* in the flow domain. Only, in most parts of the domain (away from the interface), the quantity of one of the two fluids is zero or very close to zero. The interface between the two fluids appears as a gradual transition from fluid 1 to fluid 2. In this way, in fact, the concept of an interface between the two fluids disappears from the model: it is replaced by the concept of a numerical transition layer. The interface region is not fundamentally different from the rest of the flow, only the concentration of the two fluids changes faster there than in the rest of the domain. Numerically, this is a great advantage, since no special interface model is needed to act only on the interface cells.

Each fluid still has its own density, but a single pressure and a single velocity are assumed for the two fluids, instead of two different pressures and velocities. Thus, the fluid elements do not move relative to each other. In this way, the model loses its physical two-phase behaviour: for instance, there are no longer two different sound speeds. But this behaviour is not desired anyway, as two-phase phenomena like the above do not occur in real two-fluid flow with sharp interfaces. In a numerical model, the two fluids may penetrate into each other, but by *numerical diffusion* only; they cannot convect into each other.

Concerning the interaction between the fluid elements, we do allow forces that keep the velocity of the fluid elements equal. However, we do not allow heat conduction between the elements. As the two fluids have different densities but the same pressure, they are not necessarily in thermal equilibrium. This is physically possible when heat conduction is absent.

Counting the unknown variables in these models, seven unknowns are found for the full two-phase model (two densities, two velocities, two pressures and one measure for the relative concentration of the fluids). This is consistent with the seven-equation model of Baer and Nunziato [4], used among others by Abgrall and Saurel [3, 26]. For our two-fluid model, five unknowns remain. A state vector $\boldsymbol{q}$ could be $\boldsymbol{q} = [\rho_1, \rho_2, u, p, Y]^T$, with Y a measure of the relative amount of fluid 1. To successfully integrate this model in time, we need five differential equations. Models for compressible two-fluid flow, based on less than five equations, may lose information about the flow during time integration. This may be a cause of pressure oscillations [2]. Our five differential equations are chosen in the next section.

2.2. DIFFERENTIAL EQUATIONS

To accurately solve problems with strong discontinuities, we strive for a model that is entirely based on conservation laws. In this section, suitable equations are selected. For convenience, we do this in 1D.

The standard Euler equations for single-fluid flow are derived without assumptions about the microscopic

behaviour of the flow medium, so these equations are valid for the two-fluid model too:

$$(\rho)_t + (\rho u)_x = 0, \tag{2.1a}$$
$$(\rho u)_t + \left(\rho u^2 + p\right)_x = 0, \tag{2.1b}$$
$$(\rho E)_t + (\rho E u + p u)_x = 0. \tag{2.1c}$$

However, we have to find the correct expressions for the bulk quantities ρ and E. First α, the volume fraction of fluid 1, is chosen as the variable Y. In our physical flow model, this means that a part α of a small volume dV is filled with elements of fluid 1 and a part $(1-\alpha)$ with elements of fluid 2. Therefore, a part α of the volume has the properties of fluid 1 and the remaining part $(1-\alpha)$ has the properties of fluid 2. We can use this to define any bulk quantity; the bulk density ρ and bulk total energy E are

$$\begin{aligned} \rho &= \alpha\rho_1 + (1-\alpha)\rho_2, \\ \rho E &= \alpha\rho_1 E_1 + (1-\alpha)\rho_2 E_2, \end{aligned} \tag{2.2}$$

with the total energy for each fluid defined as

$$\begin{aligned} E_1 &= e_1 + \tfrac{1}{2}u^2, \\ E_2 &= e_2 + \tfrac{1}{2}u^2. \end{aligned} \tag{2.3}$$

The symbols e denote the internal energy of the fluids.

Two more conservation laws are needed to close the system. There are no more bulk conservation laws available, so the only option is to look for conserved quantities of one of the fluids. The first one is, of course, the conservation of mass for one fluid, since the fluids are not supposed to change into each other. Let us consider conservation of mass for fluid 1. Using the partial density $\rho_1\alpha$ (as $\rho_1\alpha\,dV$ is the mass of fluid 1 in a volume dV), the corresponding equation is:

$$(\rho_1\alpha)_t + (\rho_1 u\alpha)_x = 0. \tag{2.4}$$

This equation implies that the fluid elements do not move relative to each other. Together with equation (2.1a), the equation implies mass conservation for both fluids.

For the last equation, only one option remains: an equation for the energy of fluid 1. Momentum for fluid 1, instead of energy, cannot be used: we know the bulk momentum and we know that the two fluids move at the same speed, so we already know the momentum of fluid 1 without time integration (this is shown in detail in section 3.1). So the energy equation for fluid 1 is the only possible choice. This equation has a special property: the fluid elements exert forces on each other, so they *exchange* energy. This exchange appears as a source term in the energy equation:

$$(\rho_1 E_1\alpha)_t + (\rho_1 E_1 u\alpha + pu\alpha)_x = S. \tag{2.5}$$

The remaining part of this paper is largely devoted to handling the source term. Although, in a strict mathematical sense, equation (2.5) is not in conservation form, it is a genuine conservation law for $S = 0$ (i.e., *everywhere* outside the numerical transition layer). In the remainder of this article, for convenience and because they are derived from physical conservation principles, we refer to our differential equations as a system of conservation laws.

Summarizing, the 1D system of equations is:

$$\boldsymbol{q}_t + \boldsymbol{f}_x = \boldsymbol{s}, \tag{2.6a}$$

with

$$\boldsymbol{q} = \begin{pmatrix} \rho \\ \rho u \\ \rho E \\ \rho_1\alpha \\ \rho_1 E_1\alpha \end{pmatrix}, \qquad \boldsymbol{f} = \begin{pmatrix} \rho u \\ \rho u^2 + p \\ \rho u E + pu \\ \rho_1 u\alpha \\ \rho_1 E_1 u\alpha + pu\alpha \end{pmatrix}, \qquad \boldsymbol{s} = \begin{pmatrix} 0 \\ 0 \\ 0 \\ 0 \\ S \end{pmatrix}. \tag{2.6b}$$

This system can be extended to more dimensions by adding a bulk-momentum conservation law for each additional dimension and fluxes in more directions.

2.3. PRIMITIVE VARIABLES

To close the system (2.6), equations are needed for the thermodynamic behaviour of the two fluids. These are the equations of state (EOS) for the two fluids. In their most general form, these equations are

$$\begin{aligned} p &= f_1(\rho_1, e_1), \\ p &= f_2(\rho_2, e_2). \end{aligned} \tag{2.7}$$

To keep the equations consistent with the physical model from section 2.1, *no* mixed-fluid equation of state is defined for the bulk fluid. The EOS (2.7) are valid in their respective fluid elements and, if necessary, bulk quantities can be defined as in equation (2.2).

The system of differential equations (2.6), combined with the equations of state (2.7) and the expression for S that is derived in the following chapter, is closed. It can be solved for the primitive variables, although this may require an iterative method for complex EOS.

For the ideal-gas equation of state, explicit formulas can be found for the primitive variables. If both fluids satisfy the ideal-gas law,

$$p = (\gamma - 1)\rho e, \tag{2.8}$$

with constant γ, then the total energies become:

$$\begin{aligned} \rho_1 E_1 \alpha &= \frac{1}{\gamma_1 - 1} p\alpha + \tfrac{1}{2}\rho_1 \alpha u^2, \\ \rho_2 E_2 (1-\alpha) &= \frac{1}{\gamma_2 - 1} p(1-\alpha) + \tfrac{1}{2}(\rho - \rho_1\alpha)\, u^2, \end{aligned} \tag{2.9}$$

so

$$\rho E = \left(\frac{\alpha}{\gamma_1 - 1} + \frac{1-\alpha}{\gamma_2 - 1} \right) p + \tfrac{1}{2}\rho u^2. \tag{2.10}$$

Rewriting of equation (2.9) shows that

$$\begin{aligned} p\alpha &= (\gamma_1 - 1)\left((\rho_1 E_1 \alpha) - \tfrac{1}{2}(\rho_1 \alpha)\, u^2 \right), \\ p(1-\alpha) &= (\gamma_2 - 1)\left((\rho E) - (\rho_1 E_1 \alpha) - \tfrac{1}{2}(\rho - (\rho_1 \alpha))\, u^2 \right). \end{aligned} \tag{2.11}$$

This gives as the expression for p:

$$p = (\gamma_1 - 1)\left((\rho_1 E_1 \alpha) - \tfrac{1}{2}(\rho_1 \alpha)\, u^2 \right) + (\gamma_2 - 1)\left((\rho E) - (\rho_1 E_1 \alpha) - \tfrac{1}{2}(\rho - (\rho_1 \alpha))\, u^2 \right), \tag{2.12}$$

and for α:

$$\alpha = \frac{(\gamma_1 - 1)\left((\rho_1 E_1 \alpha) - \tfrac{1}{2}(\rho_1 \alpha)\, u^2 \right)}{p}. \tag{2.13}$$

All the primitive variables are now known. The energy equations are not direction-dependent, so this procedure does not change for more dimensions. Only the kinetic energies change.

Note that for two-fluid flows with $\gamma_1 = \gamma_2 = \gamma$, the effect of $\rho_1 E_1 \alpha$ and $\rho_1 \alpha$ disappears from equation (2.12) and this equation reduces to

$$p = (\gamma - 1)\left(\rho E - \tfrac{1}{2}\rho u^2 \right), \tag{2.14}$$

the same expression as for single-fluid flow.

Chapter 3
That elusive source term

This chapter gives a derivation of the source term in the energy equation (2.5). For convenience, this is still done in 1D. In the first section, the source term is derived from physical principles. A characteristic analysis in section 3.2 shows that this source term gives the system the correct characteristic properties. The last section extends the analysis to discontinuous flow.

3.1. Derivation of the source term

The source term S in the last equation of the system (2.6) has a physical meaning. In the energy equation for fluid 1, it represents the energy that is transferred from fluid 2 to fluid 1. In Euler flow there is no heat conduction, so the fluids can only exchange energy by means of work: the work generated by the forces on the interfaces between the microscopic fluid elements.

There are two types of forces that act on the interfaces. The first are pressure forces, the second are a kind of friction forces. Regular friction forces occur in viscous flow in two or three dimensions, when fluid elements slide alongside each other. In inviscid flow, also in two-fluid flow, this force is absent. But another type of friction occurs in two-phase flow when two fluids with different velocities, at the same location, move through each other. This friction force does exist in our two-fluid flow model, albeit in a limit case. The two fluids have the same velocity, they can only maintain this if any velocity difference between the fluids causes inter-fluid friction forces that immediately make the velocities equal again. Thus, the friction forces provide instantaneous relaxation of velocity differences.

Our model is used to approximate solutions to two-fluid flow problems with sharp interfaces. This implies that the sum of pressure and friction forces between the elements, integrated over the transition layer, must be the same as the pressure force on the sharp interface in the physical two-fluid flow.

The requirement that the two fluids have the same velocity makes it possible to derive the source term in the energy equation. For this purpose, it is convenient to study the momentum equation for fluid 1 first:

$$(\rho_1 u\alpha)_t + \left(\rho_1 u^2\alpha + p\alpha\right)_x = S_M. \tag{3.1}$$

The source term S_M in this equation is the force exerted by fluid 2 on fluid 1. The magnitude of this force follows from the fact that fluid 1 always has the same velocity, and therefore the same acceleration, as the bulk fluid. Consider a small section of a 1D shock tube with height 1 (see figure 3.1). For convenience, all of fluid 1 has been lumped down at the bottom of this fluid element, but this lumped model is not really different from the microscopic-element flow model as discussed in section 2.1.

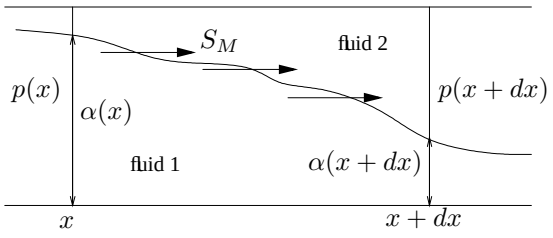

Figure 3.1: Flow element in 1D smooth flow.

The force on the entire fluid element is $p(x) - p(x+\Delta x)$. The bulk mass is $\bar{\rho}\Delta x$, with $\bar{\rho}$ the average density,

so the acceleration of the entire element becomes (using Newton's second law of motion):

$$u_t = \frac{p(x) - p(x+\Delta x)}{\bar{\rho}\Delta x}. \tag{3.2}$$

Now we study the fluid 1 part of the element. The force on this element is $(p\alpha)(x) - (p\alpha)(x+\Delta x) + S_M \Delta x$. The mass is $\overline{\rho_1\alpha}\Delta x$. The acceleration of this part is equal to the acceleration of the entire element, so

$$\frac{p(x) - p(x+\Delta x)}{\bar{\rho}\Delta x} = \frac{(p\alpha)(x) - (p\alpha)(x+\Delta x) + S_M\Delta x}{\overline{\rho_1\alpha}\Delta x} \quad \Rightarrow$$
$$\frac{\overline{\rho_1\alpha}}{\bar{\rho}} \frac{p(x) - p(x+\Delta x)}{\Delta x} = \frac{(p\alpha)(x) - (p\alpha)(x+\Delta x)}{\Delta x} + S_M,$$

and thus, in the limit for $\Delta x \downarrow 0$:

$$S_M = p\alpha_x + \alpha p_x - \frac{\rho_1\alpha}{\rho} p_x. \tag{3.3}$$

The first term, $p\alpha_x$, expresses the pressure force on the interface: pressure times the projected height of the interface. The second and third term can be combined. By introducing β, the mass fraction of fluid 1,

$$\beta = \frac{\rho_1\alpha}{\rho}, \tag{3.4}$$

this force is written as $(\alpha - \beta)p_x$. This is the friction force that keeps the velocities of the two fluids equal. For example, if for a bulk fluid $\alpha > \beta$ somewhere, then the mass of its fluid 1 there is low, but its volume is high. Therefore, fluid 1 receives a pressure force which would accelerate it faster than fluid 2, which is heavy and dense. So fluid 1 passes some of its pressure force to fluid 2, as friction. But if the two fluids have the same density ($\alpha = \beta$), each fluid gets exactly enough pressure force for equal acceleration, so the friction force vanishes. And in pure contact discontinuities ($p_x = 0$), there *is no* acceleration, which means that there the friction force vanishes too.

Now the inter-fluid force S_M is substituted back in the momentum equation (3.1):

$$(\rho\beta u)_t + \left(\rho\beta u^2 + p\alpha\right)_x = p\alpha_x + (\alpha - \beta)p_x.$$

Expansion of the left-hand side gives

$$\rho u\left(\beta_t + u\beta_x\right) + \beta\left((\rho u)_t + \left(\rho u^2 + p\right)_x\right) = 0.$$

As the two fluids have the same velocity, the mass fraction is convected with the flow, so the first term is zero. We end up with:

$$(\rho u)_t + \left(\rho u^2 + p\right)_x = 0. \tag{3.5}$$

The bulk momentum equation is recovered! As already stated in section 2.2, it is useless to integrate the momentum equation (3.1), since the momentum of fluid 1 in time follows from the bulk-fluid equations and from mass conservation for fluid 1. The only function of equation (3.1) is to determine the interface force S_M, which is used in the energy source term.

The source term S in the energy equation (2.5) is the work done by the force S_M. The velocities of the fluid elements are equal, so the velocity of the interfaces is equal to the velocity u of the elements. Therefore the work is:

$$S = S_M u = pu\alpha_x + (\alpha - \beta)\, up_x. \tag{3.6}$$

With the explicit expression (3.6) for S, the system (2.6) with (2.7) is closed. The new physical information which the source term offers, that makes the energy equation (2.5) independent while the momentum equation (3.1) is not, is the absence of heat transfer between the fluids. The kinetic energy of both fluids is fixed by requiring them to have the same velocity, but an equation for the heat transfer must be incorporated in the system to fix the internal energies of the two fluids.

3.2. CHARACTERISTIC ANALYSIS

In this section, the characteristic properties of the system (2.6), (2.7), (3.6) are studied. An analysis of the system in primitive variables shows that the source term (3.6), derived in the previous section, gives the system its physically correct characteristic wave speeds. With this source term, the Riemann invariants for the system are derived, as well as transport equations for the volume and mass fraction.

3.2.1 Five primitive equations

To facilitate analysis, the system (2.6) in conservative form is rewritten in primitive variables. Suitable primitive variables for a characteristic analysis are ρ, u, p, β and α.

Density. Start with conservation of bulk mass (equation (2.1a)):

$$\rho_t + (\rho u)_x = 0.$$

Expansion of the last term gives

$$\rho_t + \rho_x u + \rho u_x = 0. \tag{3.7}$$

Velocity. Start with conservation of bulk momentum (equation (2.1b)):

$$(\rho u)_t + \left(\rho u^2 + p\right)_x = 0.$$

Expansion, subtraction of u times equation (3.7) and division by ρ gives

$$u_t + u u_x + \frac{1}{\rho} p_x = 0. \tag{3.8}$$

Mass fraction. Start with conservation of mass for fluid 1, equation (2.4) (written using $\rho_1 \alpha = \beta \rho$):

$$(\beta\rho)_t + (\beta\rho u)_x = 0.$$

After expansion, subtraction of β times equation (3.7) and division by ρ, we find

$$\beta_t + u\beta_x = 0. \tag{3.9}$$

This result was already used in the previous section.

Pressure. The derivation of a pressure equation is rather involved, as it requires two energy equations. These are expanded first and then combined to give one equation for the pressure.

Conservation of bulk energy (equation (2.1c):

$$(\rho E)_t + (\rho u E + p u)_x = 0.$$

The total energy E can only be expressed in primitive variables with an equation of state. For this analysis, we use the EOS in its most general form (equation (2.7)), writing it as

$$\begin{aligned} e_1 &= e_1\left(p,\, \rho_1\right), \\ e_2 &= e_2\left(p,\, \rho_2\right). \end{aligned} \tag{3.10}$$

Substituting this in equation (2.2), we find

$$\rho E = \rho\left(\beta e_1 + (1-\beta) e_2 + \tfrac{1}{2} u^2\right),$$

so we can define the bulk internal energy e as:

$$e = \beta e_1 + (1-\beta)e_2. \tag{3.11}$$

With this equation, the bulk energy equation becomes

$$\left(\rho e + \tfrac{1}{2}\rho u^2\right)_t + \left(\rho e u + p u + \tfrac{1}{2}\rho u^3\right)_x = 0.$$

Expansion (using the chain rule on e), subtraction of $\left(e + \frac{1}{2}u^2 + \rho e_\rho\right)$ times equation (3.7), of ρu times equation (3.8) and of ρe_β times equation (3.9) gives the equation

$$\left(\rho e_p\right) p_t + \left(\rho e_\alpha\right) \alpha_t + \left(\rho u e_p\right) p_x + \left(\rho u e_\alpha\right) \alpha_x + \left(p - \rho^2 e_\rho\right) u_x = 0. \tag{3.12}$$

This is the first modified energy equation.

Conservation of energy for fluid 1 (equation (2.5)):

$$\left(\rho_1 E_1 \alpha\right)_t + \left(\rho_1 E_1 u \alpha + p u \alpha\right)_x = S.$$

Using the mass fraction β and substituting the EOS (3.10), this becomes:

$$\left(\beta\rho e_1 + \tfrac{1}{2}\beta\rho u^2\right)_t + \left(\beta\rho e_1 u + \alpha p u + \tfrac{1}{2}\beta\rho u^3\right)_x = S.$$

Expansion, followed by subtraction of $\beta\left(e + \frac{1}{2}u^2 + \rho e_\rho\right)$ times equation (3.7), of $\beta\rho u$ times equation (3.8) and of $\left(\rho e_1 + \frac{1}{2}\rho u^2 + \beta\rho e_{1,\rho}\right)$ times equation (3.9) gives

$$\left(\beta\rho e_{1,p}\right) p_t + \left(\beta\rho e_{1,\alpha}\right) \alpha_t + \left(\beta\rho u e_{1,p} + (\alpha-\beta)u\right) p_x + \left(\beta\rho u e_{1,\alpha} + pu\right) \alpha_x + \left(\alpha p - \beta\rho^2 e_{1,\rho}\right) u_x = S, \tag{3.13}$$

the second energy equation (note the similarity with the bulk energy equation (3.12)).

The pressure equation is found by subtracting $\frac{e_\alpha}{\beta e_{1,\alpha}}$ times equation (3.13) from equation (3.12) and multiplying by $\frac{e_{1,\alpha}}{e_p e_{1,\alpha} - e_\alpha e_{1,p}}$:

$$p_t + u p_x + \frac{\left(\beta e_{1,\alpha} - \alpha e_\alpha\right)\frac{p}{\beta\rho} + \left(e_\alpha e_{1,\rho} - e_\rho e_{1,\alpha}\right)\rho}{e_p e_{1,\alpha} - e_\alpha e_{1,p}} u_x = \frac{e_\alpha}{e_p e_{1,\alpha} - e_\alpha e_{1,p}} \frac{1}{\beta\rho}\left(u\left(\alpha-\beta\right)p_x + pu\alpha_x - S\right). \tag{3.14}$$

Volume fraction. The volume fraction equation is also found from equation (3.12). Subtracting $\frac{e_p}{\beta e_{1,p}}$ times equation (3.13) and multiplying by $\frac{e_{1,p}}{e_\alpha e_{1,p} - e_p e_{1,\alpha}}$ gives

$$\alpha_t + u\alpha_x + \frac{\left(\beta e_{1,p} - \alpha e_p\right)\frac{p}{\beta\rho} + \left(e_p e_{1,\rho} - e_\rho e_{1,p}\right)\rho}{e_\alpha e_{1,p} - e_p e_{1,\alpha}} u_x = \frac{e_p}{e_\alpha e_{1,p} - e_p e_{1,\alpha}} \frac{1}{\beta\rho}\left(u\left(\alpha-\beta\right)p_x + pu\alpha_x - S\right). \tag{3.15}$$

3.2.2 Characteristic wave speeds

Before starting the characteristic analysis, we make an assumption about the system's wave speeds. Away from the interface, the system must reduce to the single-fluid Euler equations, that are hyperbolic and have three real-valued wave speeds: information travels either with the flow or with the sound speed c relative to the flow. In the interface region, the flow medium is not fundamentally different. It is a mixture, but the two fluids have the same velocity, so they move just like a single fluid. And also in the mixture region, there is only one

sound speed. So it is reasonable to assume that the two-fluid system is hyperbolic everywhere and that its five characteristic speeds λ_m can have only three values: they are either u or $u \pm c$.

At least two wave speeds are equal to u: the first is associated with the transport of the mass fraction (equation (3.9)). The second is, in pure-fluid regions, associated with the transport of entropy (this is known from standard gas dynamics). And although it is not yet certain that entropy is convected in the mixture region too, it is impossible that a characteristic speed suddenly changes from u to $u \pm c$. Now, since the number of characteristic speeds $u - c$ is equal to the number of characteristic speeds $u + c$, we know all the λ's:

$$\lambda_1 = u - c, \qquad \lambda_{2,3,4} = u, \qquad \lambda_5 = u + c. \tag{3.16}$$

If it is to be physically correct, then the system (2.6) *must* have eigenvalues of the form (3.16).

We will now give a second derivation of the energy exchange term S, by requiring that (3.16) holds. It is shown that the source term found thus is equal to the source term found in section 3.1. The system is first-order hyperbolic so S, like the rest of the equations, contains only first-order derivatives of the primitive variables. Therefore we postulate

$$S = S_\rho \rho_x + S_u u_x + S_p p_x + S_\alpha \alpha_x + S_\beta \beta_x. \tag{3.17}$$

The terms $S_\rho, \cdots, S_\beta$ contain no derivatives. We shall derive possible expressions for these terms.

Solid-body flow. For flows with a uniform pressure p_0 and velocity u_0, the fluid moves as a solid body. This means that both the mass fraction and the volume fraction are convected with speed u_0. So when $p_x = 0$ and $u_x = 0$, the α-equation (3.15) must reduce to $\alpha_t + u\alpha_x = 0$. This implies that

$$p_0 u_0 \alpha_x - S_\rho \rho_x - S_\alpha \alpha_x - S_\beta \beta_x = 0, \quad \forall\, \rho,\, u_0,\, p_0,\, \alpha,\, \beta.$$

This requirement can only be satisfied if

$$S_\rho = 0, \qquad S_\alpha = pu, \qquad S_\beta = 0. \tag{3.18}$$

Eigenvalues of the Jacobian. The system of primitive equations is written in quasilinear form:

$$\boldsymbol{q}_t + A\boldsymbol{q}_x = 0, \tag{3.19a}$$

with

$$\boldsymbol{q} = (\rho,\, u,\, p,\, \beta,\, \alpha)^T, \tag{3.19b}$$

and the Jacobian matrix

$$A = \begin{pmatrix} u & \rho & 0 & 0 & 0 \\ 0 & u & \frac{1}{\rho} & 0 & 0 \\ 0 & U_3 & u + P_3 & 0 & 0 \\ 0 & 0 & 0 & u & 0 \\ 0 & U_5 & P_5 & 0 & u \end{pmatrix}. \tag{3.19c}$$

The abbreviations are

$$\begin{aligned} U_3 &= \frac{1}{e_p e_{1,\alpha} - e_\alpha e_{1,p}} \left((\beta e_{1,\alpha} - \alpha e_\alpha) \frac{p}{\beta\rho} - \rho \left(e_\rho e_{1,\alpha} - e_\alpha e_{1,\rho} \right) + \frac{e_\alpha}{\beta\rho} S_u \right), \\ U_5 &= \frac{1}{e_\alpha e_{1,p} - e_p e_{1,\alpha}} \left((\beta e_{1,p} - \alpha e_p) \frac{p}{\beta\rho} - \rho \left(e_\rho e_{1,p} - e_p e_{1,\rho} \right) + \frac{e_p}{\beta\rho} S_u \right), \\ P_3 &= \frac{e_\alpha}{e_p e_{1,\alpha} - e_\alpha e_{1,p}} \frac{1}{\beta\rho} \left(S_p - u\left(\alpha - \beta\right) \right), \\ P_5 &= \frac{e_p}{e_\alpha e_{1,p} - e_p e_{1,\alpha}} \frac{1}{\beta\rho} \left(S_p - u\left(\alpha - \beta\right) \right). \end{aligned} \tag{3.19d}$$

The Jacobian (3.19c) has eigenvalues

$$\lambda_1 = u + \tfrac{1}{2}P_3 - \sqrt{\frac{U_3}{\rho} + \left(\tfrac{1}{2}P_3\right)^2}, \quad \lambda_{2,3,4} = u, \quad \lambda_5 = u + \tfrac{1}{2}P_3 + \sqrt{\frac{U_3}{\rho} + \left(\tfrac{1}{2}P_3\right)^2}. \tag{3.20}$$

These eigenvalues correspond only to the form (3.16) if $P_3 = 0$, i.e., if

$$S_p = u\,(\alpha - \beta)\,. \tag{3.21}$$

Sound speed. The last term to be found is S_u. With the characteristic analysis, we cannot prove that $S_u = 0$ everywhere. However, we can show that $S_u = 0$ is a reasonable choice. We do so by considering the speed of sound. The sound speed in the eigenvalues (3.20) is $\sqrt{U_3/\rho}$, i.e.:

$$c = \sqrt{\frac{1}{e_p e_{1,\alpha} - e_\alpha e_{1,p}} \left((\beta e_{1,\alpha} - \alpha e_\alpha)\,\frac{p}{\beta\rho^2} - (e_\rho e_{1,\alpha} - e_\alpha e_{1,\rho}) + \frac{e_\alpha}{\beta\rho^2} S_u \right)}. \tag{3.22}$$

The sound speed is a thermodynamic property; it cannot depend on the velocity u. As a consequence, S_u does not depend on u. And since S_u has the dimension of pressure, given the independence of u, it cannot depend on ρ either. Thus, $S_u = S_u(p, \alpha, \beta)$ at most.

For ideal gases, using $e = \left(\frac{\alpha}{\gamma_1 - 1} + \frac{1-\alpha}{\gamma_2 - 1}\right)\frac{p}{\rho}$ and $e_1 = \frac{1}{\gamma_1 - 1}\frac{\alpha}{\beta}\frac{p}{\rho}$, equation (3.22) reduces to

$$c = \sqrt{(\alpha\gamma_1 + (1-\alpha)\gamma_2)\,\tfrac{p}{\rho} + (\gamma_2 - \gamma_1)\,\tfrac{S_u}{\rho}}. \tag{3.23}$$

In pure fluid ($\alpha = 0$ or $\alpha = 1$), it must hold $c = c_1 = \sqrt{\gamma_1 p/\rho_1}$ and $c = c_2 = \sqrt{\gamma_2 p/\rho_2}$, respectively. Moreover, if $0 < \alpha < 1$, it is reasonable to require that c lies between c_1 and c_2. The simplest choice that satisfies these requirements is $S_u = 0$. Then (3.23) reduces to

$$c = \sqrt{(\alpha\gamma_1 + (1-\alpha)\gamma_2)\,\tfrac{p}{\rho}}. \tag{3.24}$$

The sound speed (3.22) or (3.24) is used for the characteristic speeds in (3.16).

Summarizing: assuming $S_u = 0$, the only source term of the form (3.17) that

1. behaves correctly in solid-body flow and
2. gives characteristic speeds of the form (3.16)

is indeed (3.6).

3.2.3 Characteristic equations and Riemann invariants

Define the matrix L by choosing its rows to be the left eigenvectors L_i, corresponding to the eigenvalues λ_i, $i = 1, \cdots, 5$. We find that

$$L = \begin{pmatrix} 0 & -\rho c & 1 & 0 & 0 \\ -c^2 & 0 & 1 & 0 & 0 \\ 0 & 0 & 0 & 1 & 0 \\ 0 & 0 & -\frac{U_5}{\rho c^2} & 0 & 1 \\ 0 & \rho c & 1 & 0 & 0 \end{pmatrix}. \tag{3.25}$$

Then, replacing A by $L^{-1}\Lambda L$, where $\Lambda = \text{diag}(\lambda_i)$, $i = 1, \cdots, 5$, equation (3.19a) can be rewritten as

$$L\boldsymbol{q}_t + \Lambda L \boldsymbol{q}_x = 0. \tag{3.26}$$

Written out, equation (3.26) reads

$$(p_t - \rho c u_t) + (u - c)(p_x - \rho c u_x) = 0, \tag{3.27a}$$
$$(p_t - c^2 \rho_t) + u(p_x - c^2 \rho_x) = 0, \tag{3.27b}$$
$$\beta_t + u\beta_x = 0, \tag{3.27c}$$
$$\left(\alpha_t - \tfrac{U_5}{\rho c^2} p_t\right) + u\left(\alpha_x - \tfrac{U_5}{\rho c^2} p_x\right) = 0, \tag{3.27d}$$
$$(p_t + \rho c u_t) + (u + c)(p_x + \rho c u_x) = 0. \tag{3.27e}$$

These are the five characteristic equations, that define the Riemann invariants in differential form. Three of these correspond to the Riemann invariants for the single-fluid Euler equations. However, not all of them can be written in closed form.

Equations (3.27a) and (3.27e) imply that, as for single-fluid flow, $dp \pm \rho c du = 0$ along characteristics with speed $\frac{dx}{dt} = u \pm c$. Along the characteristics with speed u, the particle paths, we find with (3.27b) that $dp - c^2 d\rho = 0$. This implies that the entropy s is a Riemann invariant, just like it is for single-fluid flow. The sound speed c always satisfies $c^2 = \frac{\partial p}{\partial \rho}|_s$ (see [7]), so $dp - c^2 d\rho = 0$ means that $ds = 0$ along particle paths. The characteristic equations (3.27c) and (3.27d) are two-fluid flow equations, without a single-fluid equivalent. Equation (3.27c) implies that the mass fraction β is a Riemann invariant along the particle paths, as we have already seen. And equation (3.27d) implies that $d\alpha - \frac{U_5}{\rho c^2} dp = 0$ along these paths. For an ideal gas, this relation reads:

$$d\alpha - \frac{\alpha(1-\alpha)(\gamma_1 - \gamma_2)}{\rho c^2} dp = 0. \tag{3.28}$$

Interpreting this, we see that the second term in the left hand side is a "two-fluid perturbation term"; for $\alpha = 0$, $\alpha = 1$ or $\gamma_1 = \gamma_2$ it vanishes and the relation then states that the volume fraction α is a Riemann invariant as well. This is also the case on particle paths along which p is constant. The same can be seen if we rewrite (3.15) into a transport equation for α. For ideal gases:

$$\alpha_t + u\alpha_x = -\alpha(1-\alpha)(\gamma_1 - \gamma_2) u_x. \tag{3.29}$$

This equation has a source term: in general, α is not convected with the flow. Even if elements of the two fluids stay together (which implies that β is convected), they do not have the same change in density in reaction to an equal change in pressure: if one of the fluids compresses easier than the other fluid, then its volume fraction reduces with compression. This effect vanishes when the two fluids have equal thermodynamic properties ($\gamma_1 = \gamma_2$), when one of the fluids is absent ($\alpha = 0$ or $\alpha = 1$) or along particle paths where p is constant and hence $u_x = 0$.

3.3. Source term in discontinuous flow

The system of differential equations (2.6) is only valid in smooth flow, where the derivatives of the state variables exist. To allow discontinuities in the solution, we need a well-posed weak formulation of the system. From this formulation follows a jump condition, that describes the flow behaviour over a discontinuity.

The jump condition for any conservation law is the well-known Rankine-Hugoniot condition, which is found by integrating the conservation law over a control volume around the discontinuity:

$$[\boldsymbol{f}] = c_s [\boldsymbol{q}], \tag{3.30a}$$

with $[\ ]$ denoting the jump over the discontinuity ($[\boldsymbol{q}] = \boldsymbol{q}_R - \boldsymbol{q}_L$ etc.), c_s is the speed of the discontinuity. The first four equations in (2.6) have jump conditions of this form. But when the fifth equation is integrated over a discontinuity, the contribution of the source term depends on the internal structure of the discontinuity:

$$[\boldsymbol{f}] = c_s [\boldsymbol{q}] + \int_{x_L}^{x_R} S \, dx. \tag{3.30b}$$

This integral is not defined over a discontinuity. Most researchers [10, 14] avoid this problem by assuming an approximate shape for the discontinuity and integrating over this shape.

However, if we properly define the weak solution, then an exact integration of the integral in (3.30b) is possible. We say that a flow is a weak solution of the system (2.6) if it is the inviscid limit of solutions of (2.6) with viscous effects added. This is the normal definition of weak solutions for single-fluid flow. It guarantees that the weak solution contains no entropy-violating expansion shocks. But for two-fluid flow, the definition has another important implication: it guarantees that discontinuities have *some* internal structure. So although we do not know this structure exactly, we can apply conservation laws to a control volume that partially lies *in* the 'discontinuity' (figure 3.2). This gives expressions for the state variables, in terms of one of these state variables itself, that are continuous in the 'discontinuity'. So the source term, expressed in this variable, can be integrated. In the following, we shall write the equations in terms of the pressure.

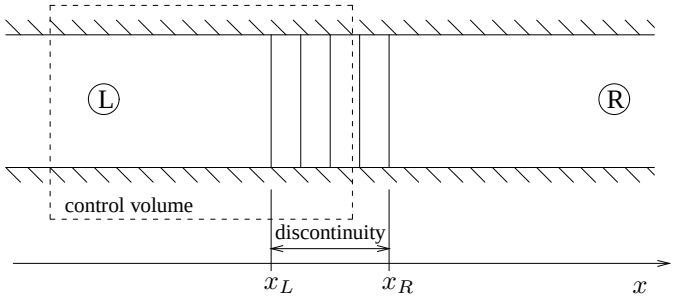

Figure 3.2: Control volume for integration across a 'discontinuity' with internal structure.

Consider the 1D shock in figure 3.2. The control volume lies between the inflow state L and the shock (this is an arbitrary choice, we can also integrate from the right). For convenience, the reference frame is fixed to the shock. We shall first derive expressions for the energy exchange $\tilde{S}_s$ and the inter-fluid force $\tilde{S}_{M_s}$ in the shock, in this reference frame ($\tilde{}$ denotes the quantities in the shock frame). Later, the source term in another reference frame, in which the shock has a velocity c_s, can be computed as

$$S_s = \tilde{S}_s + c_s \tilde{S}_{M_s}. \tag{3.31}$$

The last term appears because the source term is work, i.e, force times velocity, and the velocity is different in the other reference frame.

In the shock-fixed coordinate frame the flow is steady, so the conservation laws reduce to

$$\tilde{\boldsymbol{f}} = \tilde{\boldsymbol{f}}_L. \tag{3.32}$$

Substitution of the conservation laws (2.6) in equation (3.32) gives:

$$\rho\tilde{u} = \rho_L \tilde{u}_L \qquad \text{(bulk mass)}, \tag{3.33a}$$

$$p + \rho\tilde{u}^2 = p_L + \rho_L \tilde{u}_L^2 \quad \rightarrow \quad \tilde{u} = \tilde{u}_L - \frac{p - p_L}{\rho_L \tilde{u}_L} \qquad \text{(bulk momentum)}, \tag{3.33b}$$

$$\rho\tilde{u}\left(e + \tfrac{1}{2}\tilde{u}^2\right) + p\tilde{u} = \rho_L\tilde{u}_L\left(e_L + \tfrac{1}{2}\tilde{u}_L^2\right) + p_L\tilde{u}_L \;\rightarrow\; e = e_L - \tfrac{1}{2}\frac{p^2 - p_L^2}{\left(\rho_L\tilde{u}_L\right)^2} \qquad \text{(bulk energy)}, \tag{3.33c}$$

$$\beta\rho\tilde{u} = \beta_L\rho_L\tilde{u}_L \quad \rightarrow \quad \beta = \beta_L \qquad \text{(mass fluid 1)}. \tag{3.33d}$$

Note that the expressions (3.33) are *not* valid when the wave is a contact discontinuity. Then the velocity is zero everywhere and cannot be divided out in (3.33b) – (3.33d). However, this is no problem, as integration of (3.6) makes it immediately clear that $\tilde{S}_s = 0$ and $\tilde{S}_{M_s} = p\,[\alpha]$ in a contact discontinuity. Thus, the following derivation is for shocks only.

Force on discontinuity. The momentum equation for fluid 1 gives

$$p\alpha + \beta\rho\tilde{u}^2 = p_L\alpha_L + \beta_L\rho_L\tilde{u}_L^2 + \int_{x_L}^{x} \tilde{S}_M\, dx.$$

We substitute equation (3.33b) and rewrite the integral, using $\tilde{S}_M^* = \tilde{S}_M \frac{\partial x}{\partial p}$:

$$p\alpha + \beta_L\rho_L\tilde{u}_L\left(\tilde{u}_L - \frac{p-p_L}{\rho_L\tilde{u}_L}\right) = p_L\alpha_L + \beta_L\rho_L\tilde{u}_L^2 + \int_{p_L}^{p} \tilde{S}_M^*\, d\pi. \tag{3.34}$$

Differentiation with respect to p gives an expression for $\tilde{S}_M^*$:

$$\tilde{S}_M^* = \frac{\partial}{\partial p}(p\alpha) - \beta_L. \tag{3.35}$$

Integration of this expression (or evaluation of (3.34) for $p = p_R$) gives the total force on the discontinuity:

$$\tilde{S}_{M_s} = \int_{p_L}^{p_R} \tilde{S}_M^*\, d\pi = [p\alpha] - \beta_L\,[p]\,. \tag{3.36}$$

Energy exchange. The total energy exchange in the shock, $\tilde{S}_s$, is:

$$\tilde{S}_s = \int_{x_L}^{x_R} \tilde{u}\tilde{S}_M\, dx = \int_{p_L}^{p_R} \tilde{u}\tilde{S}_M^*\, d\pi = \int_{p_L}^{p_R} \tilde{u}\frac{\partial}{\partial p}(p\alpha)\; d\pi - \beta_L\int_{p_L}^{p_R} \tilde{u}\, d\pi. \tag{3.37}$$

The first term can be integrated by parts (as $\frac{\partial\tilde{u}}{\partial p} = -\frac{1}{\rho_L\tilde{u}_L}$). Integration of the second term is straightforward:

$$\tilde{S}_s = [p\tilde{u}\alpha] + \frac{1}{\rho_L\tilde{u}_L}\int_{p_L}^{p_R} p\alpha\, d\pi - \beta_L\tilde{u}_L\,[p] + \tfrac{1}{2}\frac{\beta_L}{\rho_L\tilde{u}_L}\,[p]^2\,. \tag{3.38}$$

So an expression for $\tilde{S}_s$ exists, which gives a unique, exact jump condition for the fifth equation:

$$\tilde{f}_R = \tilde{f}_L + \tilde{S}_s. \tag{3.39}$$

But, as opposed to the single-fluid jump conditions (of the form (3.30a)), this jump condition depends directly on the EOS of the fluids: the evaluation of the integral in (3.38) is done with help of the bulk energy equation (3.33c), which requires an EOS to be closed.

We show this derivation for the ideal-gas law. If fluid 1 and 2 are ideal gases, then (3.33c) can be rewritten as

$$\left(\frac{\alpha}{\gamma_1-1} + \frac{1-\alpha}{\gamma_2-1}\right)\frac{p}{\rho} = \left(\frac{\alpha_L}{\gamma_1-1} + \frac{1-\alpha_L}{\gamma_2-1}\right)\frac{p_L}{\rho_L} + \tfrac{1}{2}\frac{p^2-p_L^2}{\rho_L\tilde{u}_L^2}, \tag{3.40}$$

from which it follows, using (3.33a) and (3.33b), that:

$$p\alpha(p) = \left(\frac{\left(\alpha_L\frac{\gamma_2-\gamma_1}{(\gamma_1-1)(\gamma_2-1)} + \frac{1}{\gamma_2-1}\right)p_L\rho_L\tilde{u}_L + \frac{1}{2}\left(p^2-p_L^2\right)}{p_L+\rho_L\tilde{u}_L^2-p} - \frac{p}{\gamma_2-1}\right)\frac{(\gamma_1-1)(\gamma_2-1)}{\gamma_2-\gamma_1}, \tag{3.41}$$

under the constraint that $\gamma_1 \neq \gamma_2$. (For the two-fluid case $\gamma_1 = \gamma_2 = \gamma$, equation (3.41) does not yield an equation for $p\alpha$. This case will be considered later.) Integrating (3.41), it follows:

$$\begin{aligned}\int_{p_L}^{p_R} p\alpha\, dp = \\ -\tfrac{1}{2}\frac{\gamma_1-1}{\gamma_2-\gamma_1}\Bigg[\left(2\left(\frac{\gamma_2-\gamma_1}{\gamma_1-1}\alpha_L+\gamma_2\right)p_L + (\gamma_2-1)\rho_L\tilde{u}_L^2\right)\rho_L\tilde{u}_L^2\ln\left(\frac{p_L-p_R+\rho_L\tilde{u}_L^2}{\rho_L\tilde{u}_L^2}\right) \\ + \frac{\gamma_2+1}{2}p_R^2 - \frac{3\gamma_2-1}{2}p_L^2 + (\gamma_2-1)p_Lp_R + (\gamma_2-1)(p_R-p_L)\rho_L\tilde{u}_L^2\Bigg].\end{aligned} \tag{3.42}$$

Hence, with (3.42), $\tilde{S}_s$ can be evaluated.

When $\gamma_1 = \gamma_2 = \gamma$, the integration becomes much simpler. In that case, α is convected with the flow (equation (3.29)). In the discontinuity, this means that $\alpha = \alpha_L$ is constant, just like β. Thus, the integral becomes

$$\int_{p_L}^{p_R} p\alpha \, dp = \tfrac{1}{2}\alpha_L \left[p^2\right], \tag{3.43}$$

which reduces (3.38) to:

$$\tilde{S}_s = (\alpha_L - \beta_L)\left(\tilde{u}_L \left[p\right] - \frac{1}{2\rho_L \tilde{u}_L}\left[p\right]^2\right). \tag{3.44}$$

To make equation (3.38) useful in practice, it must be converted to a general reference frame, in which the shock moves. As mentioned above, this is done with equation (3.31). In the general reference frame, c_s is the shock speed and u the velocity, so

$$\tilde{u} = u - c_s, \tag{3.45}$$

in the shock frame. Upon substitution of equations (3.36), (3.38) and (3.45) in (3.31), it is found that:

$$S_s = \left[pu\alpha\right] + \frac{1}{\rho_L\left(u_L - c_s\right)}\int_{p_L}^{p_R} p\alpha \, d\pi - \beta_L u_L \left[p\right] + \tfrac{1}{2}\frac{\beta_L}{\rho_L\left(u_L - c_s\right)}\left[p\right]^2. \tag{3.46}$$

This expression is remarkably similar to (3.38).

A corresponding equation for contact discontinuities is found by substituting $\tilde{S}_s = 0$ and $\tilde{S}_{M_s} = p\left[\alpha\right]$ in (3.31):

$$S_s = c_s p\left[\alpha\right]. \tag{3.47}$$

Chapter 4
The HL^3 Riemann solver

The five-equation system is solved with a finite-volume discretisation. At the heart of this scheme is an approximate Riemann solver, the HLL solver. This particular Riemann solver does not need much characteristic information about the system and is therefore very practical for the complex five-equation model. This chapter describes the version of the solver which is used here, the combination of this solver with a second-order time integrator and the treatment of boundary conditions. For convenience, the solver is applied to single-fluid flow in this chapter. The extension to two-fluid flow and the numerical treatment of the source term are explained in the next chapter.

4.1. THE HL^3 SOLVER

The class of HLL approximate Riemann solvers is based on an idea proposed by Harten, Lax and Van Leer [12]. The output flux is an average of the exact fluxes in the Riemann solution, found by integrating the flow equations over a control volume containing the waves of the exact Riemann solution. The size of this control volume is set from estimated wave speeds. Therefore, no exact characteristic information, like Poisson expansion curves (Godunov, Osher) or characteristic speeds (Roe) is needed for the HLL solver.

The solver described here is (a simplification of) the HLL solver proposed by Linde [19]. Therefore, it is called the HLLL or HL^3 solver here.

4.1.1 Linde's HLL solver

Let us consider a system of conservation laws

$$\boldsymbol{q}_t + \boldsymbol{f}_x = 0, \tag{4.1}$$

as yet without a source term. Now we postulate a control volume that is filled with four different states, separated by three waves (figure 4.1): the outer waves λ^- and λ^+ and the middle wave V. The states $\boldsymbol{q}_L^*$ and $\boldsymbol{q}_R^*$ are assumed to be constant. The four states are connected by the integral form of the governing conservation laws (4.1):

$$\left(\lambda^+ - V\right)\boldsymbol{q}_R^* + \left(V - \lambda^-\right)\boldsymbol{q}_L^* = \lambda^+\boldsymbol{q}_R - \lambda^-\boldsymbol{q}_L - \boldsymbol{f}_R + \boldsymbol{f}_L. \tag{4.2}$$

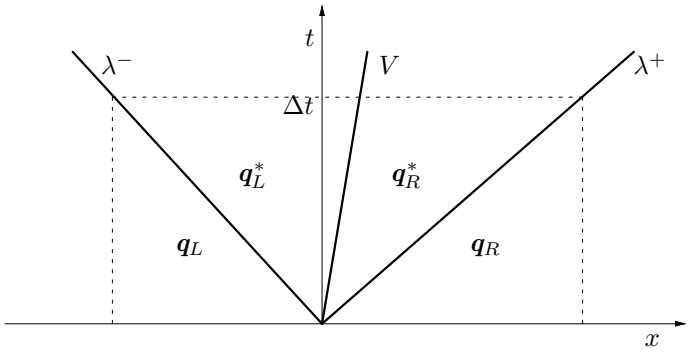

Figure 4.1: The three waves of the HL^3 solver and the domain of integration for the conservation laws.

If λ^- and λ^+ are chosen at least as big as the largest wave speeds in the exact solution of the Riemann problem, then this exact solution is contained completely in the control volume and the states $\boldsymbol{q}_L^*$ and $\boldsymbol{q}_R^*$ are both averages over a part of the exact solution. Note that, in the general case, the three waves do not represent the actual physical waves in the Riemann problem: they just divide the domain conveniently for the averaging process. The number of the physical waves does not even have to be three.

Isolated discontinuities (single shocks or contact discontinuities) in the flow can be captured with the middle wave only: in that case the outer waves have zero strength. This is a very important case, as discontinuities are isolated most of their time: they intersect only a few times in a typical problem. Linde [19] has constructed an HLL solver that sets the outer wave strengths to zero for isolated discontinuities and gives the middle wave the exact speed of the discontinuity. So in this case, the middle wave *does* represent a real wave: it models the isolated discontinuity exactly. The advantage of Linde's approach (and of the original HLL scheme) is, that *all types* of isolated discontinuities are captured with the middle wave and that no information whatsoever is needed about these discontinuities. This as opposed to, for instance, HLLC solvers that capture shocks with the *outer* waves and thus need exact expressions for the shock velocities [5, 31].

An isolated wave can be found because it satisfies the Rankine-Hugoniot condition

$$[\boldsymbol{f}] = c_s [\boldsymbol{q}], \tag{4.3}$$

with $[\boldsymbol{f}] = \boldsymbol{f}_R - \boldsymbol{f}_L$ and $[\boldsymbol{q}] = \boldsymbol{q}_R - \boldsymbol{q}_L$. If this relation holds for some c_s, then an isolated discontinuity with speed c_s is present. To reflect the idea that V models the speed of an isolated discontinuity, Linde chooses it as a weighted least-squares fit of the states and fluxes to this condition:

$$V = \frac{([\boldsymbol{q}], [\boldsymbol{f}])_P}{\|[\boldsymbol{q}]\|_P^2}, \tag{4.4}$$

with

$$([\boldsymbol{q}], [\boldsymbol{f}])_P = [\boldsymbol{q}]^T P [\boldsymbol{f}], \qquad \|[\boldsymbol{q}]\|_P^2 = [\boldsymbol{q}]^T P [\boldsymbol{q}]. \tag{4.5}$$

The matrix P is used to get the same dimensions in all the terms of the inner product.

The equation (4.2) is not enough to find the states $\boldsymbol{q}_R^*$ and $\boldsymbol{q}_L^*$. To control the strength of the middle wave, Linde *assumes* a relation

$$\boldsymbol{q}_R^* - \boldsymbol{q}_L^* = \alpha (\boldsymbol{q}_R - \boldsymbol{q}_L). \tag{4.6}$$

If $\alpha = 1$, an isolated discontinuity appears, if $\alpha = 0$, then the middle wave vanishes. So α indicates how much the solution resembles an isolated discontinuity. Therefore, α is computed in a similar way to V, with a kind of least-squares approximation. Since $V[\boldsymbol{q}]$ is the projection of $[\boldsymbol{f}]$ onto $[\boldsymbol{q}]$, the difference $[\boldsymbol{f}] - V[\boldsymbol{q}]$ is perpendicular to $V[\boldsymbol{q}]$. Therefore,

$$\frac{\|[\boldsymbol{f}] - V[\boldsymbol{q}]\|_P^2}{\|[\boldsymbol{f}]\|_P^2} + \frac{V^2 \|[\boldsymbol{q}]\|_P^2}{\|[\boldsymbol{f}]\|_P^2} = 1.$$

The last term estimates the strength of the middle wave. So Linde chooses

$$\alpha = \frac{V^2 \|[\boldsymbol{q}]\|_P^2}{\|[\boldsymbol{f}]\|_P^2} = \frac{([\boldsymbol{q}], [\boldsymbol{f}])_P^2}{\|[\boldsymbol{q}]\|_P^2 \|[\boldsymbol{f}]\|_P^2}. \tag{4.7}$$

It is easy to check, if $[\boldsymbol{q}]$ and $[\boldsymbol{f}]$ satisfy equation (4.3), that equation (4.4) gives $V = c_s$ and that equation (4.7) gives $\alpha = 1$.

The last choice to be made is the speeds of the outer waves; this choice is only important when $\alpha \neq 1$. In theory, the three-wave system must completely contain the exact Riemann solution, so the λ's must be larger than the largest wave speed in the problem. But in practice, the quality of the average decreases just as much

when the λ's are chosen too large as when they are chosen too small. So a reasonable approximation of the speed of the real outer waves works fine:

$$\begin{aligned} \lambda^+ &= \max\left(\lambda_{\max,\,L},\, \lambda_{\max,\,R},\, V\right), \\ \lambda^- &= \min\left(\lambda_{\min,\,L},\, \lambda_{\min,\,R},\, V\right). \end{aligned} \tag{4.8}$$

V is added in this expression because it approximates the shock speed in a shock wave and to make sure that the V-wave does not lie outside the λ-waves. Now all the variables in equation (4.2) are known, so the intermediate states $\boldsymbol{q}_L^*$ and $\boldsymbol{q}_R^*$ can be computed.

The output flux follows from conservation over a half plane, either $x > 0$ or $x < 0$, depending on the signs of V and the λ's:

$$\boldsymbol{f}_{HL^3} = \begin{cases} \boldsymbol{f}_L & \text{if } \lambda^- \geq 0, \\ \boldsymbol{f}_L^* = \boldsymbol{f}_L + \lambda^- \left(\boldsymbol{q}_L^* - \boldsymbol{q}_L\right) & \text{if } V \geq 0 \text{ and } \lambda^- < 0, \\ \boldsymbol{f}_R^* = \boldsymbol{f}_R + \lambda^+ \left(\boldsymbol{q}_R^* - \boldsymbol{q}_R\right) & \text{if } V < 0 \text{ and } \lambda^+ \geq 0, \\ \boldsymbol{f}_R & \text{if } \lambda^+ < 0. \end{cases} \tag{4.9}$$

Note that we do not take $\boldsymbol{f}_L^* = \boldsymbol{f}\left(\boldsymbol{q}_L^*\right)$ etc., as these fluxes do not satisfy the averaged conservation laws. Taking $\boldsymbol{f}_L^* = \boldsymbol{f}\left(\boldsymbol{q}_L^*\right)$ and $\boldsymbol{f}_R^* = \boldsymbol{f}\left(\boldsymbol{q}_R^*\right)$ would generally not give $\boldsymbol{f}_L^* = \boldsymbol{f}_R^*$ for $V = 0$, whereas (4.9) does, given (4.2).

4.1.2 Choice of P — a reality check

In the inner products (4.5), the different terms of the state and flux vectors have different dimensions. Therefore, the matrix P is used in the inner product. In the literature [12, 19], the components of P are usually based on the input states. In particular, Linde uses a convex entropy function

$$\sigma\left(\boldsymbol{q}\right) = -su, \tag{4.10}$$

with s the entropy of the system, and then takes the components of P as integrals over the second derivatives of this function

$$P = \int_0^1 \frac{\partial^2 \sigma}{\partial \boldsymbol{q}^2}\left(\theta \boldsymbol{q}_L + (1-\theta)\,\boldsymbol{q}_R\right)\, d\theta. \tag{4.11}$$

It is shown here that a much simpler choice for P works equally well.

When $\alpha = 1$, then P must be chosen such, that the middle-wave speed V equals c_s in the Rankine-Hugoniot equation (4.3). It can be easily seen from equation (4.4) that *any* P with nonzero determinant gives the correct V if $\alpha = 1$. And, as shown above, $\alpha = 1$ in most of the flow domain.

Remain only the few cases where $\alpha \neq 1$. There, the V wave has no real physical meaning, so there is no physical guideline for choosing P. Indeed, the whole background of equation (4.4), approximating the dominant wave speed in the exact Riemann problem, becomes meaningless as α approaches zero and there is no more dominant wave speed. In that case, the only thing we can require is that V is bounded somehow, so that the flux computation does not explode.

Previous researchers [12, 19] have decided that they want P to be bounded by the eigenvalues of the Roe matrix. Then they construct a P-matrix like (4.11), to be able to prove this boundedness. Doubtlessly, it is nice to have such a bound, since this means that V will never be much larger than the wave speeds in the exact Riemann problem. But a much wider range of P matrices exists, that also give a bound on V and are much easier to implement, removing the necessity to construct and differentiate an entropy function.

The easiest choice is to choose P *constant*: any constant matrix P with a nonzero determinant, for which $P^{1/2}$ exists, and with $P^{1/2}$ symmetric, gives a V which is bounded. For, if $P^{1/2}$ is symmetric, then $(P^{1/2})^T = P^{1/2}$, so

$$V = \frac{[\boldsymbol{q}]^T \left(P^{1/2}\right)^T P^{1/2}\,[\boldsymbol{f}]}{[\boldsymbol{q}]^T \left(P^{1/2}\right)^T P^{1/2}\,[\boldsymbol{q}]} = \frac{\left(P^{1/2}\,[\boldsymbol{q}]\right)^T \left(P^{1/2}\,[\boldsymbol{f}]\right)}{\left(P^{1/2}\,[\boldsymbol{q}]\right)^T \left(P^{1/2}\,[\boldsymbol{q}]\right)}.$$

Both the numerator and the denominator in the above expression are standard inner products. The numerator satisfies the Cauchy-Schwarz inequality:

$$|V| = \frac{\left|\left(P^{1/2}\left[\boldsymbol{q}\right]\right)^T\left(P^{1/2}\left[\boldsymbol{f}\right]\right)\right|}{\left\|P^{1/2}\left[\boldsymbol{q}\right]\right\|^2} \leq \frac{\left\|P^{1/2}\left[\boldsymbol{q}\right]\right\|\left\|P^{1/2}\left[\boldsymbol{f}\right]\right\|}{\left\|P^{1/2}\left[\boldsymbol{q}\right]\right\|^2} = \frac{\left\|P^{1/2}\left[\boldsymbol{f}\right]\right\|}{\left\|P^{1/2}\left[\boldsymbol{q}\right]\right\|}. \tag{4.12}$$

So V is bounded by the length of $[\boldsymbol{f}]$, divided by the length of $[\boldsymbol{q}]$, under the constant mapping $P^{1/2}$.

In practice, the result of a flow computation does not depend much on the choice of P. In figure 4.2, solutions are shown for two 1D shock tube problems. The conservation laws are the single-fluid Euler equations, with ideal gases. A first-order accurate solver is used, to get the greatest possible effect from the Riemann solver. A solution with Linde's P-matrix (4.11) is compared with a solution using the simplest possible constant P,

$$P = I \qquad \text{with appropriate units.} \tag{4.13}$$

There is almost no visible difference between the solutions. In other problems with near-vacuum conditions, the constant P proved to be a more robust choice than Linde's P. Therefore, the identity matrix is a practical choice for P. It will be used later on.

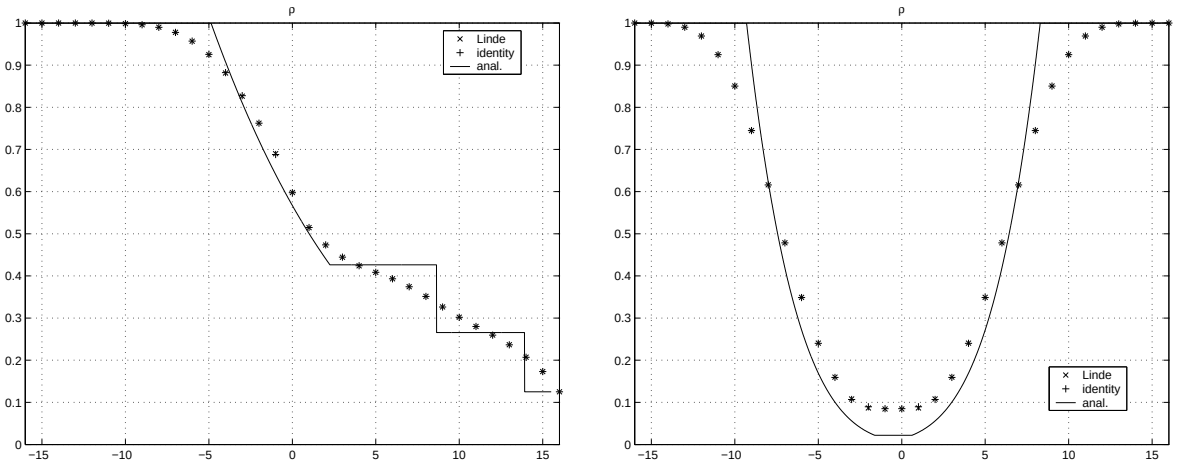

a) b)

Figure 4.2: Effect of different P matrices on the solution of 1D problems. Linde's matrix is compared with $P = I$. Sod problem with 33 cells, 32 time steps (a), 123 problem with 33 cells, 16 time steps (b). $\Delta t/\Delta x = 0.2$ in both cases. (For a description of the problems, see Toro [31]).

4.1.3 Entropy condition

Weak solutions of the Euler equations may contain expansion shocks, which violate the second law of thermodynamics, because the entropy decreases across such a shock. Therefore, a Riemann solver must contain an entropy condition that prevents expansion shocks. An example is the entropy condition of Harten, Lax and Van Leer:

$$[\rho us] - c_s\left[\rho u\right] \geq 0. \tag{4.14}$$

This equation states that, in a reference frame in which the shock is not moving, the entropy flux out of the shock is equal to or larger than the flux into the shock. This condition allows contact discontinuities too: the

flow in the neighbourhood of a contact discontinuity has a uniform speed, so the speed in the discontinuity-fixed frame is zero. Therefore, both fluxes are zero and the entropy condition is satisfied.

Linde [19] sets $\alpha = 0$ whenever condition (4.14) is violated, thus creating a large numerical viscosity which breaks entropy-violating shocks. In principle, this is a good idea, but it has a drawback, because the jump $[\boldsymbol{q}_i]$ across a small part of a single isentropic wave satisfies the Rankine-Hugoniot relations up to $\mathcal{O}([\boldsymbol{q}_i]^2)$. This can be seen as follows:

Consider a small jump $[\boldsymbol{q}_i]$ in a single isentropic wave. From gasdynamics it is known that the difference between this jump and a jump $[\boldsymbol{q}_d]$ across a discontinuity, for which one of the components (like the velocity jump) is the same, is small:

$$[\boldsymbol{q}_i] = [\boldsymbol{q}_d] + \mathcal{O}([\boldsymbol{q}_{i,d}]^3),$$

with $\mathcal{O}([\boldsymbol{q}_{i,d}])$ denoting the order of magnitude of the jump, which is the same for the isentropic and the discontinuity jump. Now consider the jump in the flux. The flux is a smooth function of the state (even in discontinuities), so we may expand with the Jacobian matrix A:

$$\begin{aligned}
[\boldsymbol{f}_d] &= A\,[\boldsymbol{q}_d] + \mathcal{O}([\boldsymbol{q}_{i,d}]^2),\\
[\boldsymbol{f}_i] &= A\,[\boldsymbol{q}_i] + \mathcal{O}([\boldsymbol{q}_{i,d}]^2) = A\left([\boldsymbol{q}_d] + \mathcal{O}([\boldsymbol{q}_{i,d}]^3)\right) + \mathcal{O}([\boldsymbol{q}_i]^2) = A\,[\boldsymbol{q}_{i,d}] + \mathcal{O}([\boldsymbol{q}_{i,d}]^2).
\end{aligned}$$

In both cases, we start from the same state, so the same A is valid. Substituting the Rankine-Hugoniot condition $[\boldsymbol{f}_d] = c_s\,[\boldsymbol{q}_d]$ yields

$$[\boldsymbol{f}_i] = c_s\,[\boldsymbol{q}_d] + \mathcal{O}([\boldsymbol{q}_{i,d}]^2) = c_s\,[\boldsymbol{q}_i] + \mathcal{O}([\boldsymbol{q}_{i,d}]^2).$$

A more detailed analysis shows that the isentropic jump satisfies (4.3) with a c_s equal to the characteristic speed $u \pm c$.

So on a cell face in an expansion wave, the best choice for α that the HL^3 solver can make is $\alpha = 1$ (isolated wave). This is also the *only* choice for α that does not violate the entropy condition: in an expansion wave, the entropy must remain constant, but in that expansion, all three waves of the HL^3 solver are entropy-decreasing expansion shocks. The output flux, however, is computed from the jump across one of the outer waves only (equation (4.3)). So if this wave has strength zero, the HL^3 flux is equal to the pure upwind flux and the entropy in the flux is equal to the (uniform) entropy in the cells. The only way to get outer waves with strength zero is to give the middle wave maximum strength, i.e., set $\alpha = 1$.

Remains the problem of expansion shocks. Moving expansion waves cause no problems, as expansion shocks are smeared here by the numerical viscosity in the scheme and then spread more because of the divergent characteristics. The only problems appear when $|u| = c$, or when $M = 1$ (figure 4.3a). In that case, one of the characteristics does not move and an expansion shock may appear. This shock can be easily broken by setting $\alpha = 0$ in a sonic point,

$$|u| = c, \tag{4.15}$$

when the relevant characteristics diverge,

$$\begin{aligned}
u_L - c_L &< u_R - c_R \qquad \text{for } u > 0,\\
u_L + c_L &< u_R + c_R \qquad \text{for } u < 0.
\end{aligned} \tag{4.16}$$

The effect of this choice is seen in figure 4.3b. Both the Linde technique ($\alpha = 0$ in the entire expansion) and the new condition remove the large expansion shock, although the new technique does show a small wiggle at $M = 1$. An advantage of the new technique is that it does not enforce $\alpha = 0$ when the expansion wave meets a contact discontinuity, thus keeping the contact discontinuity sharp.

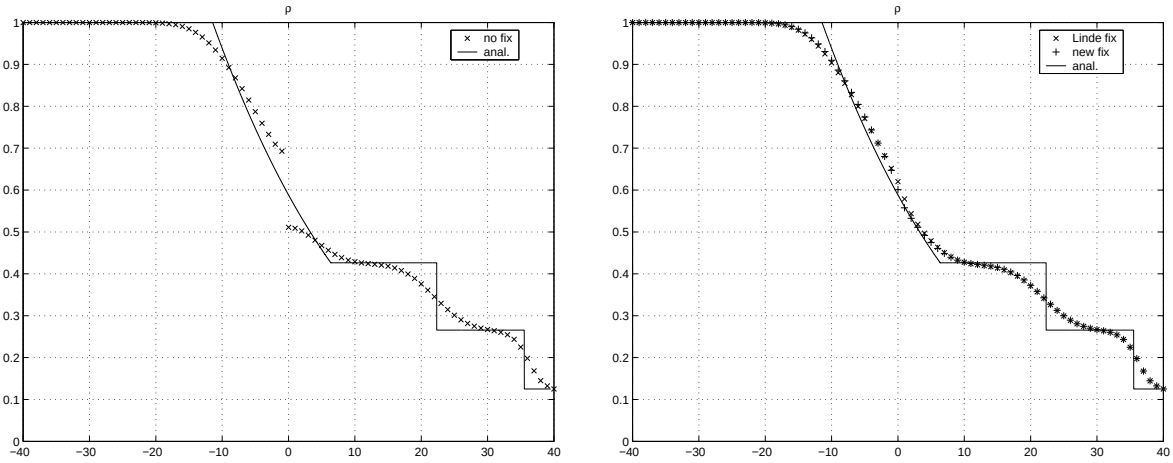

a) b)

Figure 4.3: Effect of entropy conditions. Sod problem with initial speed 0.5. 81 cells, 80 time steps. No entropy condition (a), Linde and new entropy condition (b). $\sigma = 0.2$.

4.1.4 Fixes for zero state jump

In section 4.1.2 we showed that V is properly defined for $[\boldsymbol{q}] \neq 0$. But we still have to define V for $[\boldsymbol{q}]$ very close to zero. At that moment, V is not important, we just do not want a division by zero in equation (4.4). So this equation is modified:

$$V = \frac{([\boldsymbol{q}], [\boldsymbol{f}])_P}{\|[\boldsymbol{q}]\|_P^2 + \epsilon}, \tag{4.17}$$

for a small positive constant ϵ. This means that $V \to 0$ for $[\boldsymbol{q}]$ approaching zero. Since small $[\boldsymbol{q}]$ may appear in weak expansion waves, we want α to be 1 for $[\boldsymbol{q}]$ going to zero. So equation (4.7) is modified as:

$$\alpha = \frac{([\boldsymbol{q}], [\boldsymbol{f}])_P^2 + \epsilon}{\|[\boldsymbol{q}]\|_P^2 \, \|[\boldsymbol{f}]\|_P^2 + \epsilon}. \tag{4.18}$$

Some care must be taken when ϵ is chosen: an ϵ that is too big causes wiggles in the solution. This problem can be removed completely by letting α go to zero for small $[\boldsymbol{q}]$, but this creates unnecessary smearing of stationary interfaces.

4.2. Second-order accuracy

In order to obtain accurate solutions on reasonably coarse meshes, a higher-order discretisation of the flow equations is required. The combination of this discretisation with the HL^3 solver is not straightforward: Linde [19] reported problems with higher-order reconstructions of the cell face states. This section describes the second-order discretisation used here and addresses some of the problems that arise when this discretisation is combined with the HL^3 solver.

4.2.1 Second-order limited scheme

The discretisation used here is a combination of a limited upwind reconstruction of the cell face states with a two-step time integrator, comparable to Richtmyer's scheme. It was developed by the authors [33, 34] to be combined easily with unsteady grid adaptation techniques.

The time integration is done in two steps: starting from a state $\boldsymbol{q}^k$, a first-order accurate time step is made

first. The resulting state is used to compute a second-order accurate flux for the second step:

$$\begin{aligned} \boldsymbol{q}_i^{k+1} &= \boldsymbol{q}_i^k - \tfrac{\Delta t}{\Delta x}\left(\boldsymbol{f}_{i+\frac{1}{2}}^k - \boldsymbol{f}_{i-\frac{1}{2}}^k\right), \\ \boldsymbol{q}_i^{k+2} &= \boldsymbol{q}_i^k - 2\tfrac{\Delta t}{\Delta x}\left(\boldsymbol{f}_{i+\frac{1}{2}}^{k+1} - \boldsymbol{f}_{i-\frac{1}{2}}^{k+1}\right). \end{aligned} \tag{4.19}$$

An advantage of this scheme is, that it does not need a different scheme for the first time step. Stability of the scheme is proved for CFL-numbers below 0.25, but in practice, higher CFL-numbers give stable solutions too [33].

Reconstruction of the cell face states $\boldsymbol{q}_L$ and $\boldsymbol{q}_R$, the input for the Riemann solver, is done with the standard limiting technique [29]:

$$\begin{aligned} q_{L,i+\frac{1}{2}}^p &= q_i^p + \tfrac{1}{2}\phi(r_L)\left(q_i^p - q_{i-1}^p\right), \qquad \text{with} \quad r_L = \frac{q_{i+1}^p - q_i^p}{q_i^p - q_{i-1}^p}, \\ q_{R,i+\frac{1}{2}}^p &= q_{i+1}^p + \tfrac{1}{2}\phi(r_R)\left(q_{i+1}^p - q_{i+2}^p\right), \qquad \text{with} \quad r_R = \frac{q_i^p - q_{i+1}^p}{q_{i+1}^p - q_{i+2}^p}. \end{aligned} \tag{4.20}$$

The limiting is done individually for each component q^p of $\boldsymbol{q}$. Several choices are possible for the nonlinear limiter function $\phi(r)$. Here, we use the $\kappa = \frac{1}{3}$ limiter, proposed by Koren [16]. This limiter follows the third-order accurate (in 1D) $\kappa = \frac{1}{3}$ scheme of Van Leer [18] as much as possible:

$$\phi_K(r) = \begin{cases} 0 & r < 0, \\ 2r & 0 \le r < \frac{1}{4}, \\ \frac{2}{3}r + \frac{1}{3} & \frac{1}{4} \le r < \frac{5}{2}, \\ 2 & r \ge \frac{5}{2}. \end{cases} \tag{4.21}$$

This limiter works well in combination with the HL^3 solver. A test on the Sod problem with the second-order scheme (figure 4.4) shows that the $\kappa = \frac{1}{3}$ limiter gives lower errors than the well-known minmod ($\phi = \min(1, \max(0, r))$) and Van Albada ($\phi = \frac{r^2+r}{r^2+1}$) limiters.

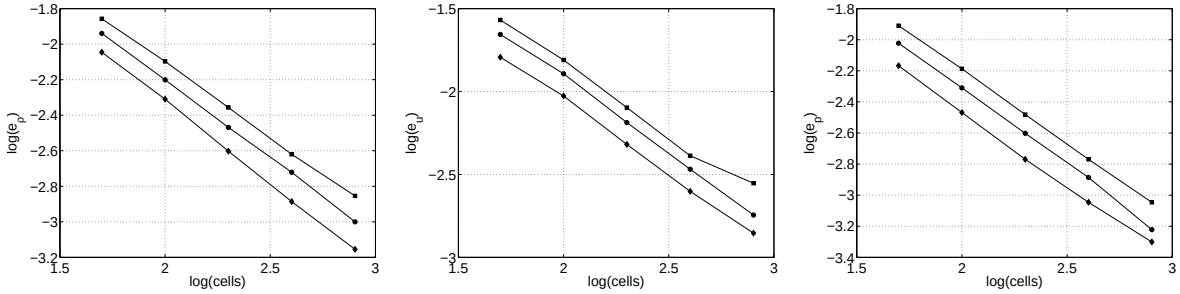

Figure 4.4: L^1-errors in second-order accurate solution of Sod problem, for three limiters. Different grid sizes, $\Delta t/\Delta x = 0.25$. ■: Minmod limiter, ●: Van Albada limiter, ♦: $\kappa = 1/3$ limiter.

4.2.2 HL^3 and limited variables

The input states that the limiter (4.20) generates for the Riemann solver do not necessarily make sense. For a first-order method, the input states $\boldsymbol{q}_L$ and $\boldsymbol{q}_R$ are the states in the neighbouring cells, that follow directly from the time integration. This means that the input states are consistent with the solution, so the resulting Riemann problems correspond to parts of the real solution of the problem. For higher-order methods, this is no longer true. The input states follow from component-wise interpolation between the cells. These interpolations are

not the same for all components, so the limited states may not be consistent with the actual problem (although they are, of course, close to the real solution).

For the HL^3 solver, this results in widely oscillating values of V, combined with values of α that do not approach 1. Figure 4.5 gives an example: V for a first- and second-order accurate solution of Sod's problem. The first-order V correctly resembles the local wave speeds (left to right: expansion fan, contact discontinuity and shock), while the second-order V is a total mess.

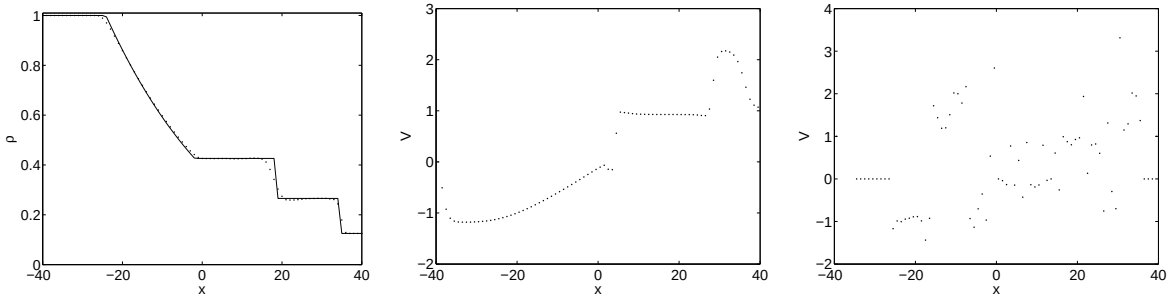

Figure 4.5: Solution of the Sod problem, on 80 cells, 80 time steps, $\Delta t/\Delta x$ = 0.25. Left to right: density, V for first-order solution and V for second-order solution.

However, in second-order solutions, the only places where the Riemann solver is important are the discontinuities. In smooth flow, the reconstructed left and right state at a cell face are more or less equal. So the Riemann problem there consists of very weak waves, that do not cause errors, even if they are inconsistent with the actual problem.

The limiting process does not guarantee that the discontinuities are handled well, the accuracy of the solution greatly depends on the state variables q^p that are limited. Here, three state vectors are considered. They are (for single-fluid flow):

1. Primitive variables: $\boldsymbol{q} = (\rho,\, u,\, p)$,
2. Conservative variables: $\boldsymbol{q} = (\rho,\, \rho u,\, \rho E)$,
3. Riemann invariants: $\boldsymbol{q} = (u,\, c,\, z)$, with $c = \sqrt{\gamma \frac{p}{\rho}}$ and $z = \ln\left(\frac{p}{\rho^\gamma}\right)$.

These three choices have a different behaviour in discontinuities.

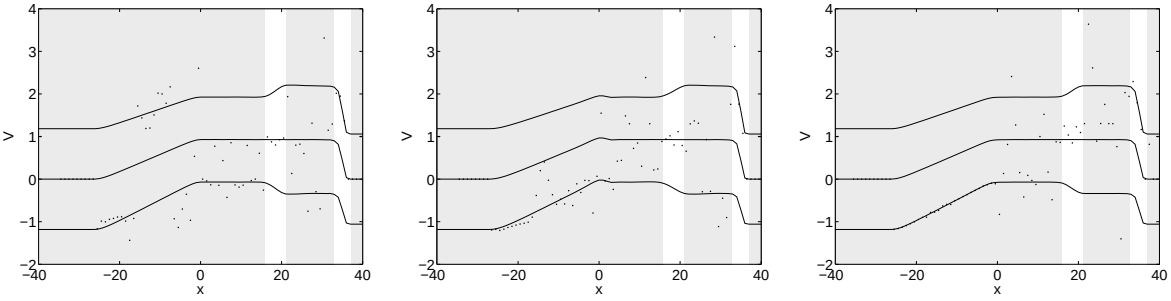

Figure 4.6: V in second-order solutions of Sod's problem, with three different state vectors for limiting. Left to right: primitive, conservative and Riemann variables. The V-values are compared with the three characteristic speeds, which are (bottom to top): $u - c$, u and $u + c$.

If they work properly they reconstruct, in a discontinuity, a series of Riemann problems that resembles the discontinuity. For the HL^3 solver, this means that α approaches 1 on each interface in the discontinuity and that V is the speed of the discontinuity. So let us study the V-distribution of figure 4.5 again. Figure 4.6 gives V for the three different sets of reconstructed variables. These V-values are compared with the computed values of the three characteristic speeds: $u-c$, u and $u+c$. Now we see that the chaotic behaviour mostly appears in the regions where the flow is smooth: the smaller $[\boldsymbol{q}]$ is, the larger the influence of small disturbances. In fact, the discontinuities are resolved well: all methods follow the line $u+c$ in the shock (the primitive reconstruction is the best, the conservative reconstruction has a large overshoot). The methods approach the line u in the contact discontinuity. Here the primitive reconstruction is clearly the best. Note, by the way, how well the Riemann reconstruction performs in the expansion, though this is irrelevant as the flow is smooth there.

Error plots for the three different reconstructions (figure 4.7) show that the Riemann-variable reconstruction gives the lowest errors, though not much lower than the primitive-variable reconstruction. The conservative-variable reconstruction gives inferior performance.

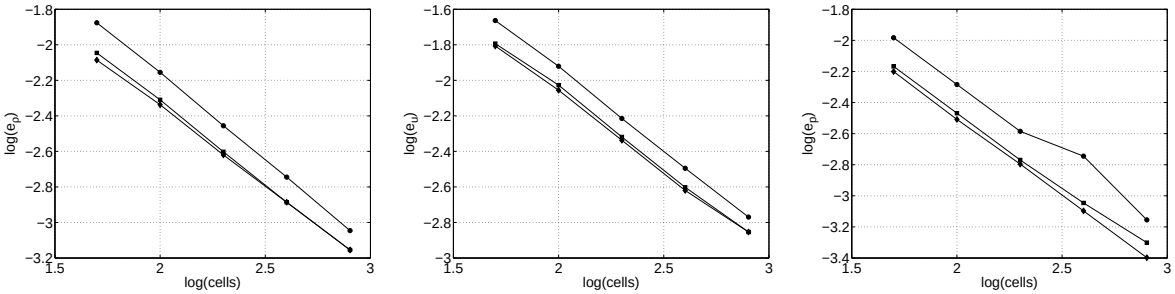

Figure 4.7: L^1-errors in second-order accurate solution of Sod problem, for three sets of limited variables. Different grid sizes, $\Delta t/\Delta x = 0.25$. ■: primitive variables, ●: conservative variables, ♦: Riemann invariants.

The Riemann-variable reconstruction is generally considered to be the best choice. But this reconstruction has one great disadvantage: it completely fails in strong contact discontinuities, *independent* of the choice of the Riemann solver. The problem is that, in a flow with constant p and u, the limited states (the input for the Riemann solver) must also have this pressure and velocity. The velocity u is limited directly, but the pressure is a combination of c and z:

$$p = \left(\frac{c^\gamma}{\gamma^\gamma e^z} \right)^{\frac{1}{\gamma-1}}.$$

The c and z in each limited state must yield the same p always, which is impossible if they are limited independently. A numerical test confirms this problem (figure 4.8): the pressure in a contact discontinuity, computed with the Riemann-variable reconstruction, is not constant. Reconstruction in primitive variables, on the other hand, works well. Here, both u and p are limited directly, so they remain constant.

Concluding: the primitive-variable reconstruction is best suited for problems with strong contact discontinuities, like the two-fluid problems studied here. Therefore, it is used further on, in combination with the two-fluid model. There, it has an additional advantage, which will be explained in section 5.2.

4.3. Boundary conditions

The treatment of boundary conditions for HLL solvers is a non-trivial problem. In most high-accuracy Riemann solvers, like Godunov or Osher, the Riemann flux is based on a physical wave pattern, so boundary conditions can be found by studying the same physical problem, if a number of conditions are specified, e.g., inflow pressure and velocity. But the HL^3 solver, on the other hand, does not have a physical wave system, so physical reasoning cannot be used to find relevant boundary conditions.

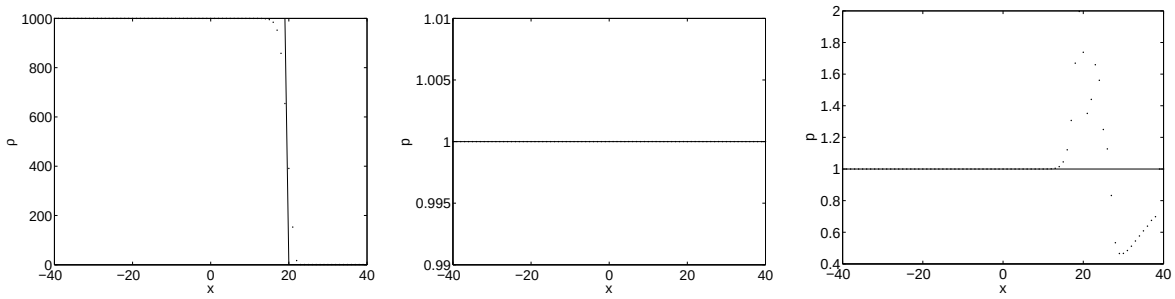

Figure 4.8: Second-order solution of a moving contact discontinuity. Left to right: density and pressure with primitive-variable reconstruction, pressure with Riemann-variable reconstruction.

However, there is a simple method to find boundary conditions: using virtual cells behind the boundary and computing the boundary fluxes by applying the normal HL^3 solver to the reconstructed inner boundary cell face and to the virtual cell state. The only thing left to decide is the state $\boldsymbol{q}_B$ in the virtual cell:

Inflow – outflow. In inflow and outflow boundaries, it is easiest to specify a full boundary state $\boldsymbol{q}_B$. Then the Riemann solver decides for itself how much of this information it uses, from everything (supersonic inflow) to nothing (supersonic outflow).

Wall. At a wall we want zero velocity. This can be achieved by choosing $\boldsymbol{q}_B$ equal to the reconstructed state on the inner cell face, but with the sign of the normal velocity component changed. In this way, the normal velocity in the HL^3 flux is always zero.

The advantage of this approach is that it is very easy to implement. A disadvantage is that we cannot control which boundary conditions are prescribed on each boundary, since the Riemann solver selects these. The actual boundary conditions may be unphysical. It appears, from numerical tests, that this makes the boundaries sensitive to instability, especially when the velocity at the boundary is zero. Some correction is often necessary.

Chapter 5
Numerical treatment of the source term

The previous chapter described the second-order accurate numerical discretisation that is used here, for single-fluid flow. The two-fluid flow model from the first two chapters resembles single-fluid flow so much (no interface model is needed, etc.), that the numerical discretisation requires only one addition to solve it: a discretisation of the source term.

By integrating equation (2.6) over a cell, a basic equation for a finite-volume discretisation is found:

$$\frac{\partial}{\partial t}\int_{\Omega_i} \boldsymbol{q}\,dx + \left(\boldsymbol{f}_{i+\frac{1}{2}} - \boldsymbol{f}_{i-\frac{1}{2}}\right) = \int_{\Omega_i} \boldsymbol{s}\,dx. \tag{5.1}$$

Physically speaking, the fifth equation in (5.1) says that the increase rate of the energy of fluid 1 is equal to the energy that flows in with fluid 1 over the boundaries (the flux), plus the energy that is passed from fluid 2 to fluid 1 in the cell (the source term). Thus, the source term appears as an integral over the cell. A numerical evaluation of this integral must be added in the time integration. Furthermore, the source term influences the computation of the fluxes. Both these aspects are treated in the following sections.

5.1. HL^3 FOR TWO-FLUID FLOW

In principle, the fluxes and the source term are different things. As equation (5.1) shows, the source term is created *in* the cell, while the fluxes are inflow over the boundaries. But the HL^3 solver defines the fluxes by integration of the system of flow equations, which contains the source term. Therefore, some treatment of the source is needed to find the HL^3 flux. Here, we show first how the HL^3 solver is modified to incorporate a source term and then how the source term in discontinuities, from section 3.3, is treated numerically.

5.1.1 A source term in the HL^3 solver

Integrating the system (2.6) over a control volume as in figure 4.1, we get an equation that is equivalent to (4.2):

$$\left(\lambda^+ - V\right)\boldsymbol{q}_R^* + \left(V - \lambda^-\right)\boldsymbol{q}_L^* = \lambda^+\boldsymbol{q}_R - \lambda^-\boldsymbol{q}_L - \boldsymbol{f}_R + \boldsymbol{f}_L + \frac{1}{\Delta t}\int_0^{\Delta t}\int_{\lambda^-\Delta t}^{\lambda^+\Delta t} \boldsymbol{s}\,dx\,dt. \tag{5.2}$$

As all the areas in figure 4.1 have a constant state, the source term is zero there. Across each wave, the source term is a constant, so the integral reduces to a summation:

$$\frac{1}{\Delta t}\int_0^{\Delta t}\int_{\lambda^-\Delta t}^{\lambda^+\Delta t} \boldsymbol{s}\,dx\,dt = \boldsymbol{s}_{\lambda^-} + \boldsymbol{s}_V + \boldsymbol{s}_{\lambda^+} = \Sigma\boldsymbol{s}. \tag{5.3}$$

We do not yet write an exact expression for $\Sigma\boldsymbol{s}$, this is done in section 5.1.2.

Apart from the conservation laws, the HL^3 scheme is not changed. The expressions (4.4) for V and (4.7) for α are kept, as is the estimate for the outer waves (4.8). Only, the equation (3.22) is used for the mixed-fluid sound speed. For simplicity, we set the fifth diagonal component of P to zero,

$$P = \text{diag}\left(\begin{bmatrix}1 & 1 & 1 & 1 & 0\end{bmatrix}\right). \tag{5.4}$$

In this way, no problems arise with the source term, it can be computed after V if necessary. We still capture all waves, because shocks, expansions and contact discontinuities all show up in the first four equations. And although this P is singular, $\|[\boldsymbol{q}]\|_P$ can never become 0 for nonzero $[\boldsymbol{q}]$, so V cannot blow up.

So, combining these equations, we find the inner states:

$$\begin{aligned} \boldsymbol{q}_L^* &= \frac{\lambda^+ \boldsymbol{q}_R - \lambda^- \boldsymbol{q}_L - \Delta \boldsymbol{f} - (\lambda^+ - V)\,\alpha \Delta \boldsymbol{q} + \Sigma \boldsymbol{s}}{\lambda^+ - \lambda^-}, \\ \boldsymbol{q}_R^* &= \boldsymbol{q}_L^* + \alpha\,(\boldsymbol{q}_R - \boldsymbol{q}_L)\,. \end{aligned} \tag{5.5}$$

The inner fluxes follow again from conservation over a half plane:

$$\begin{aligned} \boldsymbol{f}_L^* &= \boldsymbol{f}_L + \lambda^-\,(\boldsymbol{q}_L^* - \boldsymbol{q}_L) + \boldsymbol{s}_{\lambda^-} \qquad \text{if } V \geq 0, \\ \boldsymbol{f}_R^* &= \boldsymbol{f}_R + \lambda^+\,(\boldsymbol{q}_R^* - \boldsymbol{q}_R) - \boldsymbol{s}_{\lambda^+} \qquad \text{if } V < 0. \end{aligned} \tag{5.6}$$

Finally, the output flux is selected as in equation (4.9), i.e.,

$$\boldsymbol{f}_{HL^3} = \begin{cases} \boldsymbol{f}_L & \text{if } \lambda^- \geq 0, \\ \boldsymbol{f}_L^* & \text{if } V \geq 0 \text{ and } \lambda^- < 0, \\ \boldsymbol{f}_R^* & \text{if } V < 0 \text{ and } \lambda^+ \geq 0, \\ \boldsymbol{f}_R & \text{if } \lambda^+ < 0. \end{cases} \tag{5.7}$$

5.1.2 Approximate source term

To use the HL^3 solver, an approximation of the source term in the three waves, i.e., $\boldsymbol{s}_{\lambda^-}$, $\boldsymbol{s}_V$ and $\boldsymbol{s}_{\lambda^+}$, is needed. The HL^3 solver is rather simple and contains non-physical waves, which means that two problems appear in the numerical approximation of the source term. These are discussed below. In more advanced Riemann solvers, based on physical waves only, these problems disappear.

First, the artificial discontinuities that appear in the HL^3 solver do not always satisfy the Rankine-Hugoniot relation (it was found in section 4.1.1, that $\boldsymbol{f}_L^*$ is not equal to $\boldsymbol{f}\,(\boldsymbol{q}_L^*)$). Therefore, several relations applied in the derivation of the source term (3.46) in discontinuities (e.g. that β is constant in a shock) are not valid in the HL^3 discontinuities. Therefore, some modifications must be made to (3.46), before it can be combined with the HL^3 solver.

The problem with this modification is that (3.46) contains terms of a completely different character, that are supposed to cancel each other exactly in most cases (e.g. the friction contribution must be zero when $\alpha = \beta$). It is very hard to change the terms in (3.46) such, that they allow general discontinuities and still vanish correctly when necessary. Numerical experiments showed that most formulations lead to instability and large errors.

And second, the inner states $\boldsymbol{q}_L^*$ and $\boldsymbol{q}_R^*$ are not necessarily physically consistent: the conservative state vectors satisfy the conservation law (5.2), but do not always give sensible values when they are converted to primitive variables (e.g, there is no guarantee that $\boldsymbol{q}_L^*$ and $\boldsymbol{q}_R^*$ have $0 \leq \alpha \leq 1$). Therefore, it is difficult to compute separate source terms for the three HL^3 waves, since the source terms are expressed in primitive variables.

Summarizing: the best choice for a source term to be combined with the HL^3 solver is to use one equation for the entire source term $\Sigma \boldsymbol{s}$ and to choose an expression that is as simple and robust as possible.

The numerical source term is based on equation (3.37):

$$S_s = \int_{x_L}^{x_R} u S_M \, dx = \bar{u} S_{M_s}, \tag{5.8}$$

for some average $\bar{u}$. For S_{M_s}, there is the expression (3.36), for $\bar{u}$ we simply use the upwind velocity:

$$S_s \approx \begin{cases} u_L\,([p\alpha] - \beta_L\,[p]) & V \geq 0, \\ u_R\,([p\alpha] - \beta_R\,[p]) & V < 0. \end{cases} \tag{5.9}$$

Then the HL^3 source becomes

$$\Sigma \boldsymbol{s} = [0,\, 0,\, 0,\, 0,\, S_s]^T\,. \tag{5.10}$$

For the individual waves, we assume that the strength of the source term in each wave corresponds to the strength of the wave itself, so

$$\begin{aligned} \boldsymbol{s}_V &= \alpha\Sigma\boldsymbol{s}, \\ \boldsymbol{s}_{\lambda^-} &= \boldsymbol{s}_{\lambda^+} = \frac{1-\alpha}{2}\Sigma\boldsymbol{s}. \end{aligned} \tag{5.11}$$

Numerical tests show that this choice works well.

5.2. Time integration

Discretising the time derivative in the conservation law (5.1) as in (4.19), a two-step scheme is found for the two-fluid system:

$$\begin{aligned} \boldsymbol{q}_i^{k+1} &= \boldsymbol{q}_i^k - \tfrac{\Delta t}{\Delta x}\left(\boldsymbol{f}_{i+\frac{1}{2}}^k - \boldsymbol{f}_{i-\frac{1}{2}}^k\right) + \tfrac{\Delta t}{\Delta x}\boldsymbol{s}_i^k, \\ \boldsymbol{q}_i^{k+2} &= \boldsymbol{q}_i^k - 2\tfrac{\Delta t}{\Delta x}\left(\boldsymbol{f}_{i+\frac{1}{2}}^{k+1} - \boldsymbol{f}_{i-\frac{1}{2}}^{k+1}\right) + 2\tfrac{\Delta t}{\Delta x}\boldsymbol{s}_i^{k+1}. \end{aligned} \tag{5.12}$$

The source term $\boldsymbol{s}_i^k$ in this expression is the total energy passed from fluid 2 to fluid 1 in cell i, at time level k:

$$\boldsymbol{s}_i^k = \int_{x_i-\frac{\Delta x}{2}}^{x_i+\frac{\Delta x}{2}} \boldsymbol{s}(x,t^k)\,dx. \tag{5.13}$$

For higher-order methods, the state is discontinuous near the cell faces and smooth, but non-constant, in the cells. So the source from equation (5.13) consists of two parts:

1. Source in the discontinuities at the cell faces,
2. Source in the smooth flow in the cell.

These sources are summed to get $\boldsymbol{s}_i^k$.

The source term in the discontinuities is created in the waves of the Riemann problems at the cell faces. The usual model for a Godunov-type discretisation is as in figure 5.1a: the flow is discontinuous at the cell faces, at the beginning of a time step. So Riemann problems appear at the cell faces and the waves of these Riemann problems run into the cells. As a model for these waves, we use the three waves of the HL^3 solver, that were used to compute the fluxes. Each wave produces a source term: $\boldsymbol{s}_{\lambda^-}$, $\boldsymbol{s}_V$ and $\boldsymbol{s}_{\lambda^+}$. These sources must be taken into account for the time integration, the source in a wave contributes to the source of the cell in which the wave is running. In figure 5.1a, the source in cell i comes from the V- and λ^+-waves at $i-\frac{1}{2}$ and from the λ^--wave at $i+\frac{1}{2}$.

Note that these sources are *not* incorporated in the fluxes, even though they are computed with the Riemann solver and appear in the flux formulas (5.6): the fluxes are the flow through the cell faces, they are the same for

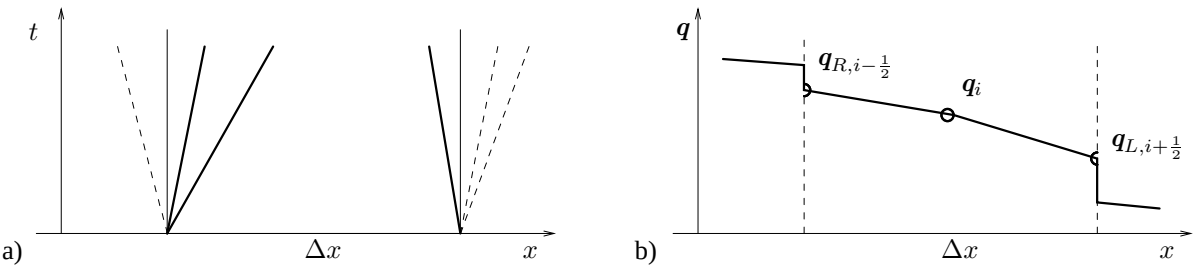

Figure 5.1: Source term in a cell: from cell faces (a) and internal flow (b).

the two cells of the cell face. The sources however, are produced *in* the cells, albeit near the interface, and are not equal for two neighbour cells.

In higher-order methods, the state in a cell is not constant, so a source appears in the smooth flow inside the cell. As we compute the source term at the very beginning of each time step (at time k for the first time step and at time $k+1$ for the second time step), the waves from the cell faces have only moved an infinitesimal distance into the cell. Therefore, the state in the cell interiors is still continuous and the source term can easily be found by integrating the differential source term (3.6):

$$S_{i,\,\text{cont}} = \int_{x_i - \frac{\Delta x}{2}}^{x_i + \frac{\Delta x}{2}} \left(pu\alpha_x + (\alpha - \beta)\, p_x\right) dx. \tag{5.14}$$

The state in a cell for the second-order scheme follows from the limiter: the resulting state variables are piecewise linear functions (figure 5.1b). If the limiter is applied to the primitive variables ρ, u, p, α and β, then the integration of (5.14) is easy. For three general, linear variables a, b and c,

$$\begin{aligned} &a(x) = a_i + (a_j - a_i)\frac{x - x_i}{x_j - x_i}, \quad b(x) = b_i + (b_j - b_i)\frac{x - x_i}{x_j - x_i}, \quad c_x = \frac{c_j - c_i}{x_j - x_i} \quad \Longrightarrow \\ &\int_{x_i}^{x_j} abc_x\, dx = \left(\tfrac{1}{3}\left(a_i b_i + a_j b_j\right) + \tfrac{1}{6}\left(a_i b_j + a_j b_i\right)\right)\left(c_j - c_i\right). \end{aligned} \tag{5.15}$$

Applying this integral to (5.14), we find that:

$$\begin{aligned} S_{i,\,\text{cont}} = {} & \left(\tfrac{1}{3}\left(p_R u_R + p_i u_i\right) + \tfrac{1}{6}\left(p_R u_i + p_i u_R\right)\right)\left(\alpha_i - \alpha_R\right) \\ & + \left(\tfrac{1}{3}\left((\alpha-\beta)_R u_R + (\alpha-\beta)_i u_i\right) + \tfrac{1}{6}\left((\alpha-\beta)_R u_i + (\alpha-\beta)_i u_R\right)\right)\left(p_i - p_R\right) \\ & + \left(\tfrac{1}{3}\left(p_i u_i + p_L u_L\right) + \tfrac{1}{6}\left(p_i u_L + p_L u_i\right)\right)\left(\alpha_L - \alpha_i\right) \\ & + \left(\tfrac{1}{3}\left((\alpha-\beta)_i u_i + (\alpha-\beta)_L u_L\right) + \tfrac{1}{6}\left((\alpha-\beta)_i u_L + (\alpha-\beta)_L u_i\right)\right)\left(p_L - p_i\right). \end{aligned} \tag{5.16}$$

Here p_R means $p_{R,\,i-\frac{1}{2}}$, p_L means $p_{L,\,i+\frac{1}{2}}$ etc. This source term is added to the wave source terms to get $\boldsymbol{s}_i^k$ or $\boldsymbol{s}_i^{k+1}$.

Chapter 6
Numerical results

The two-fluid model from the previous chapter is applied to a series of 1D and 2D test problems. The aim of the method is to provide conservative and pressure-oscillation free solutions. The results in this chapter show that the method indeed gives good capturing of shock waves and continuous pressure over the two-fluid interfaces.

6.1. 1D RESULTS

The method is first tested on three 1D shock tube problems. The problems have analytical solutions, so the numerical solutions can be compared with these exact solutions.

All tests are Riemann problems. In these problems, the shock tube is divided in two by a membrane at $x = 0$. The membrane separates two gases that have different states, but the state in each gas is constant. When the membrane is removed at $t = 0$, a pressure wave (either a shock or an expansion fan) runs into each gas. The interface between the gases moves too, depending on the velocity between the pressure waves.

All fluids are ideal gases, their equation of state is (2.8). But, as the problems are two-fluid, the γ's on each side of the interface are not equal.

6.1.1 Contact discontinuity

The first test is a contact discontinuity of water–air density ratio. In this case, the two gases have the same pressure and velocity, so no pressure waves appear, only the interface is convected. The solution in figure 6.1 shows that the interface is numerically smeared, but that its center lies exactly in the correct location. And, most importantly, the pressure is constant: no pressure oscillations occur. Thus, the method treats interfaces exactly as desired.

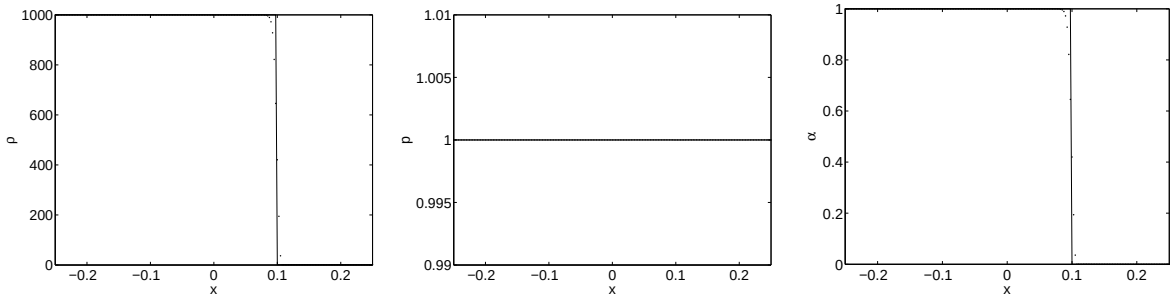

Figure 6.1: 1D contact discontinuity. $p = 1$, $u = 1$, $\rho_L = 1000$, $\rho_R = 1$, $\gamma_L = 1.4$ and $\gamma_R = 1.6$. The grid has 200 cells, 80 time steps and $\Delta t/\Delta x = 0.5$ (CFL = 0.5). Solid lines: exact solution.

6.1.2 High-pressure Sod

The second test is a two-fluid variation of Sod's problem: the two gases are at rest, the left gas has a higher pressure and density than the right gas. The current problem has a ten times higher left pressure and density than the original Sod problem, giving it a pressure ratio of 100:1. The solution consists of a left-running expansion fan, a right-running shock and the, right-moving, two-fluid interface.

Figure 6.2 shows that the discontinuities (shock and two-fluid interface) are in the proper locations. Note that the pressure is constant over the contact discontinuity and that the volume fraction is constant over the shock and over the expansion fan. Even in this difficult case, no pressure oscillations appear.

A convergence study for this particular problem, on five grids, shows that the L^1-errors in ρ, u and p converge approximately with the power 0.96 of the mesh width (see table 6.1). The volume fraction converges with the power 0.78 of the mesh width. This rate of convergence is comparable with that for single-fluid solutions with limited second-order schemes.

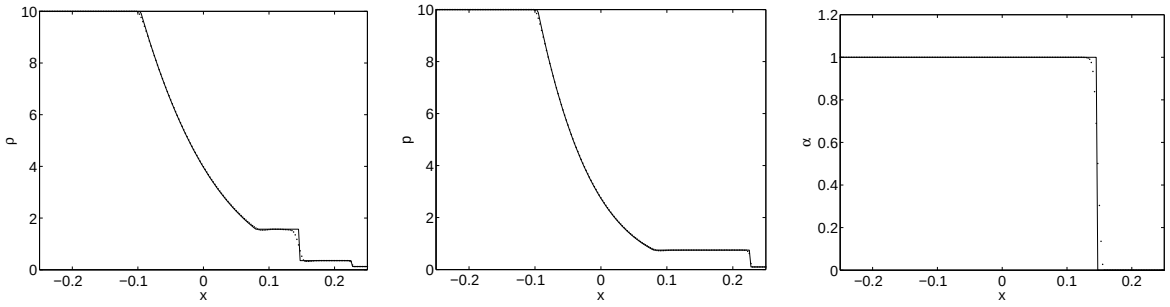

Figure 6.2: High-pressure, two-fluid Sod problem. $(\rho, u, p)_L = (10,\ 0,\ 10)$, $(\rho, u, p)_R = (0.125,\ 0,\ 0.1)$, $\gamma_L = 1.4$ and $\gamma_R = 1.6$. The grid has 200 cells, 160 time steps, $\Delta t/\Delta x = 0.2$ (CFL = 0.56). Solid lines: exact solution.

n	e_ρ	e_u	e_p	e_α
50	0.0804	0.0306	0.0538	0.0237
100	0.0426	0.0230	0.0264	0.0160
200	0.0221	0.0079	0.0124	0.0079
400	0.0117	0.0062	0.0068	0.0049
800	0.0062	0.0021	0.0032	0.0029
Conv. order	0.93	0.96	1.01	0.78

Table 6.1: High-pressure Sod problem: L^1-errors in four state variables on five different grids and average order of convergence for these errors.

6.1.3 No-reflection problem

The last problem is the hardest. This Riemann problem is equivalent to a strong shock wave (pressure ratio 1:100) in the left gas, hitting the interface at $t = 0$. The pressure and velocity jump over the shock are chosen such, that the shock continues in the right gas, without creating a reflection wave. So the left pressure wave in the Riemann problem has strength zero.

In the results (figure 6.3) we see the effect of the numerical approximation to the source term (see section 5.1.2). A wiggle is visible in the pressure plot, a small wave that is reflected to the left. But unlike a real pressure oscillation, this wiggle reduces in size on grid refinement. The other flow features, the transmitted shock and the two-fluid interface, are captured very well. And note that the pressure wiggle has no effect at all on the volume fraction, which is still exactly 1 away from the interface.

A convergence test in table 6.2 confirms the gradual disappearance of the pressure wiggle. The solution converges normally, with an order of approximately 1. This is exactly as expected for a problem with very heavy shocks.

6.2. 2D SHOCK–BUBBLE INTERACTION

To test the method for 2D problems, two related test cases are considered: the impact of a shock in air on a bubble of a lighter and a heavier gas. These tests are based on experiments by Haas and Sturtevant [11],

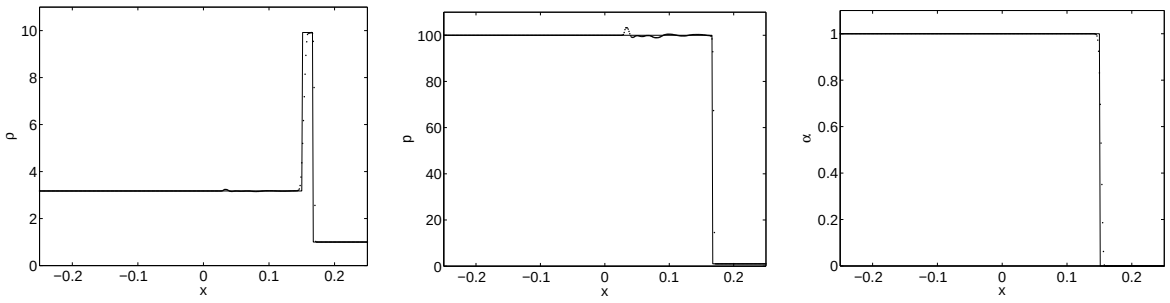

Figure 6.3: Strong shock hitting an interface, without creating a reflection wave. $(\rho, u, p)_L = (3.1748,\ 9.4350,\ 100)$, $(\rho, u, p)_R = (1,\ 0,\ 1)$, $\gamma_L = 1.667$ and $\gamma_R = 1.2$. The grid has 400 cells, 320 time steps, $\Delta t/\Delta x = 0.04$ (CFL = 0.42). Solid lines: exact solution.

n	e_ρ	e_u	e_p	e_α
100	0.2579	0.1638	1.3904	0.0220
200	0.1722	0.1126	1.0183	0.0119
400	0.0860	0.0604	0.5684	0.0053
800	0.0375	0.0218	0.2121	0.0029
1600	0.0246	0.0146	0.1422	0.0018
Conv. order	0.90	0.93	0.88	0.93

Table 6.2: No-reflection problem: L^1-errors in four state variables on five different grids and average order of convergence for these errors.

who also give an excellent analysis of the flow phenomena that appear. Numerical computations are reported, among others, by Quirk and Karni [23], Marquina and Mulet [20] and Schroll and Svensson [27].

The test setup is drawn schematically in figure 6.4. It is a shock tube with a square cross-section, in which a cylinder of a very thin cellulose film is placed. The cylinder is filled with some gas and then a shock wave is sent through the tube. When it reaches the cylinder, the shock tears the microfilm apart and then interacts with the cylindrical gas bubble. This interaction happens so fast (for a 343 m/s sound speed, the shock passes the bubble in about 10^{-4}s) that the gases do not mix much during the interaction. Therefore, the problem can be treated as a two-fluid problem.

The wave pattern depends strongly on the density of the gas in the bubble. However, some waves always appear. Initially, the shock coming from the air just continues to travel in the bubble, we call this the refracted shock wave. Another wave, the reflected wave, travels from the interface back in the air. At later times, the interaction becomes more complicated: the refracted wave leaves the bubble and continues in air as the transmitted wave, causing secondary reflected waves in the bubble as it hits the bubble interface.

The two bubble gases used in the test are helium and Refrigerant R22, a heavy gas. Both these and the air are modeled as ideal gases. Their gas properties are given in table 6.3, together with the initial conditions for the problem. These are chosen such, that the undisturbed air has a sound speed 1 (instead of 343 m/s in the experiment, but that is just a scaling matter). The shock has a Mach number of 1.22.

The experimenters observed that the helium in their cylinder was contaminated with air, because of air leakage through the microfilm, prior to the experiment. They estimated this contamination at 28 mass % air. Following Quirk and Karni, this mixture is modeled as a single ideal gas, with a higher density than pure helium (0.25463 instead of 0.19317) and a lower γ (1.648 instead of 1.667). Contamination of the R22 was considered negligible.

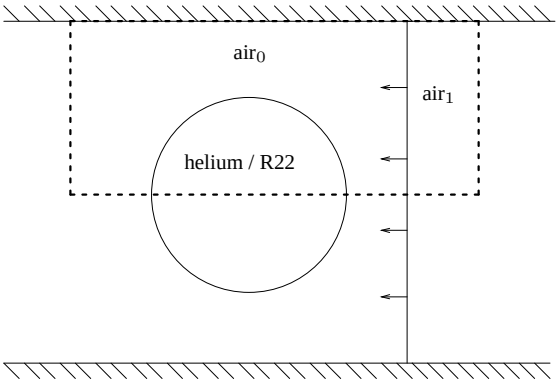

Figure 6.4: Shock in air in a shock tube, hitting a cylinder of helium or R22. The computational domain is drawn dashed.

All tests were computed on a half bubble (figure 6.4). The grid has square cells, 400 in x-direction and 200 in y-direction. The time step is $\Delta t = 2.5 \times 10^{-5}$ for the R22 case and $\Delta t = 1.25 \times 10^{-5}$ for the helium case, because the wave speeds in helium are higher than in R22.

	γ	ρ	u	v	p	α
air$_0$	1.4	1.40000	0.00000	0.00000	1.00000	1
air$_1$	–	1.92691	0.33361	0.00000	1.56980	1
helium	1.648	0.25463	0.00000	0.00000	1.00000	0
R22	1.249	4.41540	0.00000	0.00000	1.00000	0

Table 6.3: Shock hitting bubble: gas properties and initial conditions.

6.2.1 R22 bubble

Refrigerant R22 ($CHClF_2$) is an HCFC, commonly used in air conditioners and heat pumps. It was introduced to replace the ozone-depleting CFC's, but is now considered to cause unacceptable ozone-depletion itself and is scheduled for phaseout in 2020. It is a heavy gas, with a low sound speed of 0.532 in the current test.

Because of the low sound speed in R22, the refracted wave travels slowly too, lagging behind the incoming shock in air (see figure 6.5). Thus, the refracted wave becomes curved inwards. The reflected wave is initially a shock wave; after some time it starts 'climbing' up the incoming shock. An analytical analysis ascertaining almost all aspects of this initial interaction is found in appendix II. The two vertical waves behind the incoming shock are startup waves caused by the shock. These waves are not physical and may be ignored, as they are very weak and do not influence the rest of the solution. At later times, the shock in air curves inwards too, while the refracted wave is curved even further. In the last picture, the refracted wave has developed a sharp bend, with an expansion fan originating from it. Another interesting feature in the last picture is the reflected shock, which reflects from the top of the shock tube and hits the bubble again, from above.

Pressure and volume fraction plots (figure 6.6) confirm the conclusions from the 1D tests. The flow pattern seen in the density plots is split perfectly in a pressure part and the interface. Apart from some very small wiggles that disappear on grid refinement, the pressure is continuous over the interface. The two-fluid interface itself is sharp and the pressure waves are not visible in the volume fraction. One problem is visible in the last picture: there is a split in the two-fluid interface. This is probably caused by the troubles that the Riemann-solver approach has in coping with shear layers.

The speeds of the waves at the centerline of the bubble ($y = 0$) can be measured from a series of pictures of the flow. Three quantities were measured and compared with results from the experiment [11] and from the

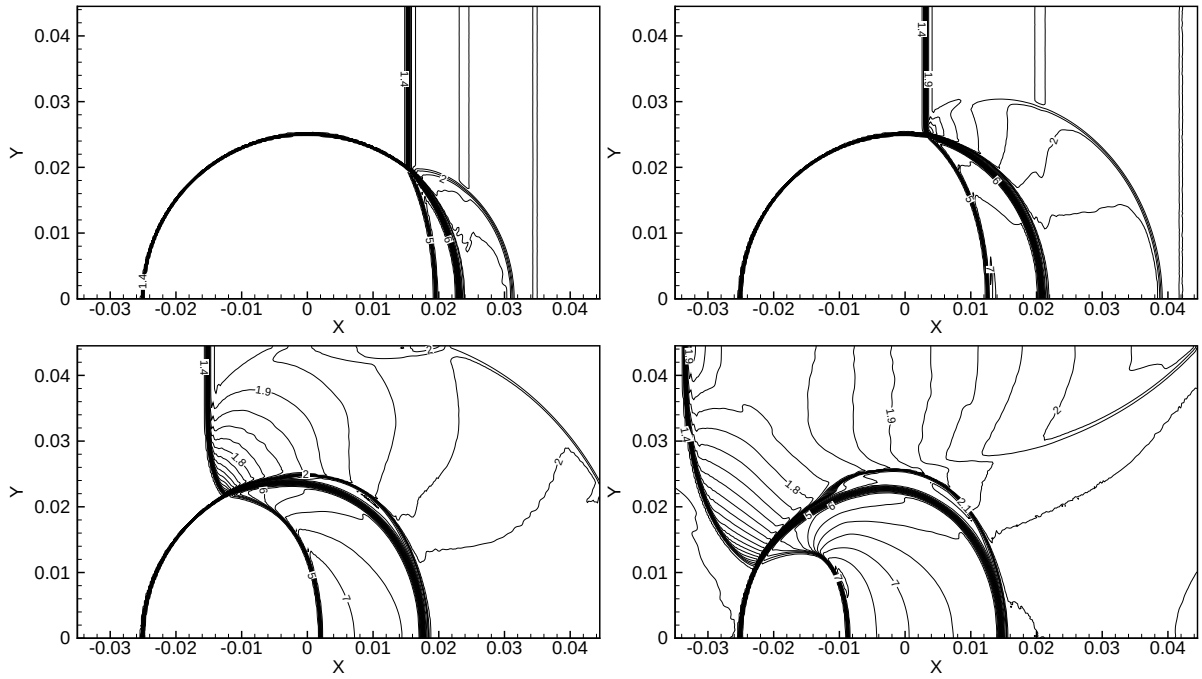

Figure 6.5: Shock hitting R22 bubble, density at $t = 7.74 \times 10^{-3}$, $t = 17.74 \times 10^{-3}$, $t = 32.74 \times 10^{-3}$, and $t = 47.74 \times 10^{-3}$.

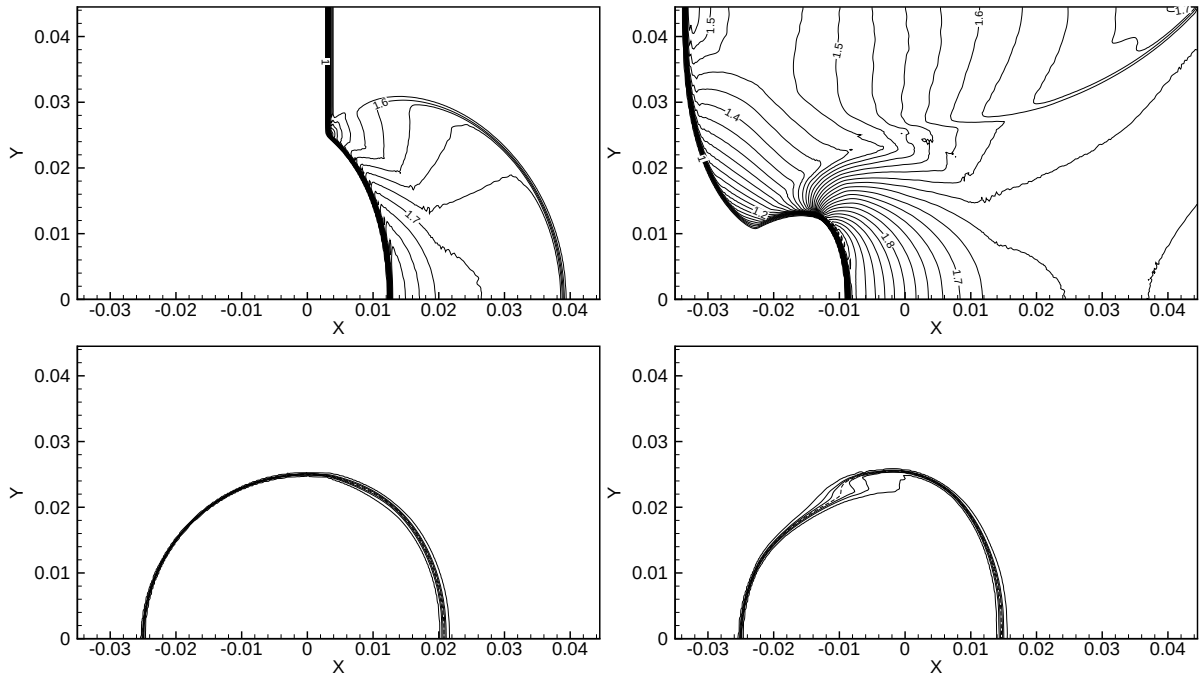

Figure 6.6: Shock hitting R22 bubble, pressure (above) and volume fraction (below) at $t = 17.74 \times 10^{-3}$ and $t = 47.74 \times 10^{-3}$.

numerical computations of Quirk and Karni [23], obtained on a very fine, adapted grid (see table 6.4). The present results were scaled with a sound speed in air of 343 m/s, valid in air at sea level and at 293 K. The measured velocities are the speed of the incoming shock c_s, the speed of the refracted shock c_r, and the speed of the two-fluid interface at the right-hand side of the bubble u_{ri}. The similarity with the other data is good, considering among others the difficulty of defining the location of a smeared shock. Especially the similarity with the experiment is remarkably good.

	c_s (m/s)		c_r (m/s)		u_{ri} (m/s)	
Present method	419	–	241	–	75	–
Quirk & Karni	420	(0.2)	254	(5.4)	70	(6.7)
Experiment	415	(1.0)	240	(0.4)	73	(2.7)

Table 6.4: Centerline wave speeds in R22 bubble test: comparison of present method with computations by Quirk and Karni [23] and experiment by Haas and Sturtevant [11]. The difference with the present method in % is given in brackets. c_s: incident shock speed, c_r: shock speed in bubble, u_{ri}: right side of interface speed.

6.2.2 Helium bubble

Helium, even if it is contaminated with air, has a much higher sound speed than air itself (2.544 in this test). Therefore, the refracted wave runs ahead of the incoming wave, curving outwards (see figure 6.8). At some point, the refracted wave moves so fast, that it runs ahead of the point where the incoming shock hits the interface. An oblique shock appears in the air, behind the refracted shock: the transmitted shock. This shock interacts with the incoming shock and crosses it, continuing on the right of the incoming shock. Finally, an expansion fan appears at the point where the incoming shock hits the interface: this expansion 'eats' the transmitted shock, turning it into an expansion wave. The flow pattern is sketched in figure 6.7.

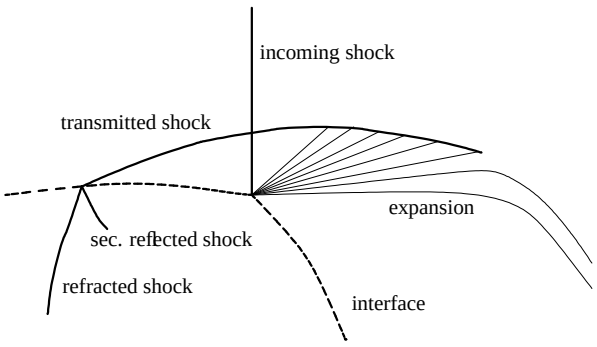

Figure 6.7: Wave pattern of the shock – helium interaction.

A secondary reflected shock starts in the corner between the refracted and the transmitted shock. This shock develops into a cusp-like shock and increases in size when the refracted shock has fully left the bubble. Then the transmitted shock has become a curved shock in a semi-circle around the bubble. The initial part of this shock–bubble interaction can be explained well with an analytical approach. Appendix II gives the analysis for the air–helium bubble as well.

The pressure and volume fraction plot, figure 6.9, shows again a perfect splitting of the pressure waves and the interface. The shocks and the interface remain very sharp. And it is interesting to see that the right side of the interface is bending inwards in the last picture. This phenomenon continues at later times, until the bubble is totally split in two vortices.

Centerline wave speeds were measured in the same way as for the R22 bubble, they are given in table 6.5. The agreement with the other data is here even closer than in the R22 case. The only noticeable exception is

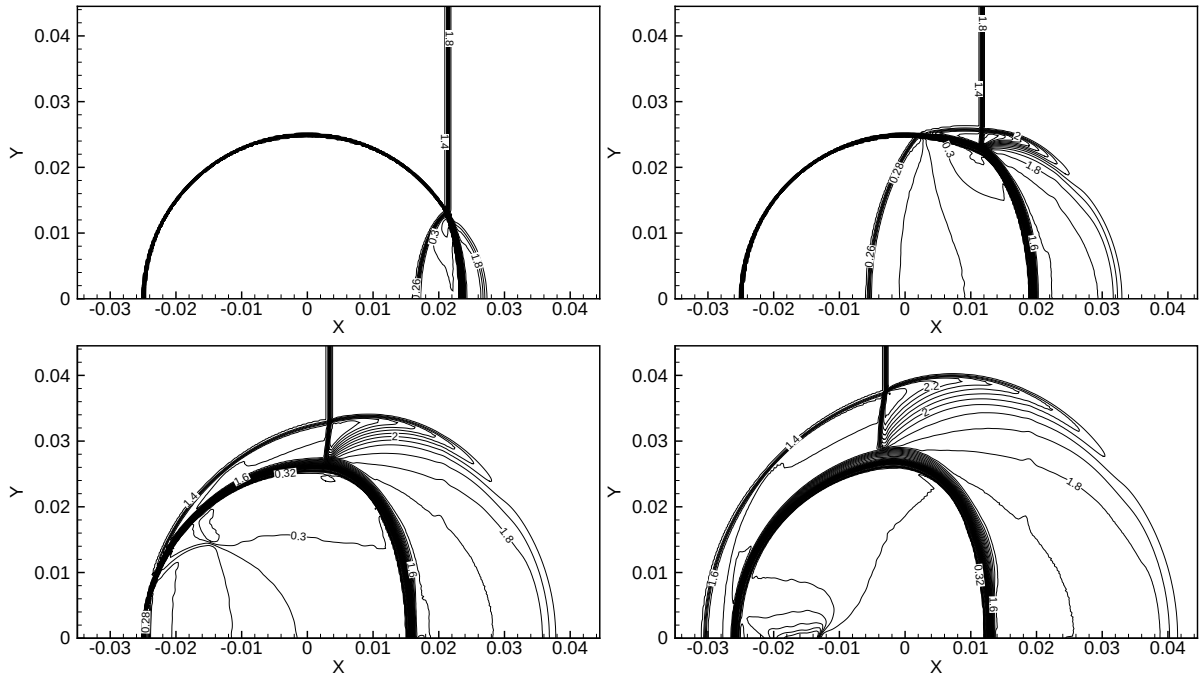

Figure 6.8: Shock hitting helium bubble, density at $t = 2.74 \times 10^{-3}$, $t = 10.74 \times 10^{-3}$, $t = 17.54 \times 10^{-3}$. and $t = 22.74 \times 10^{-3}$.

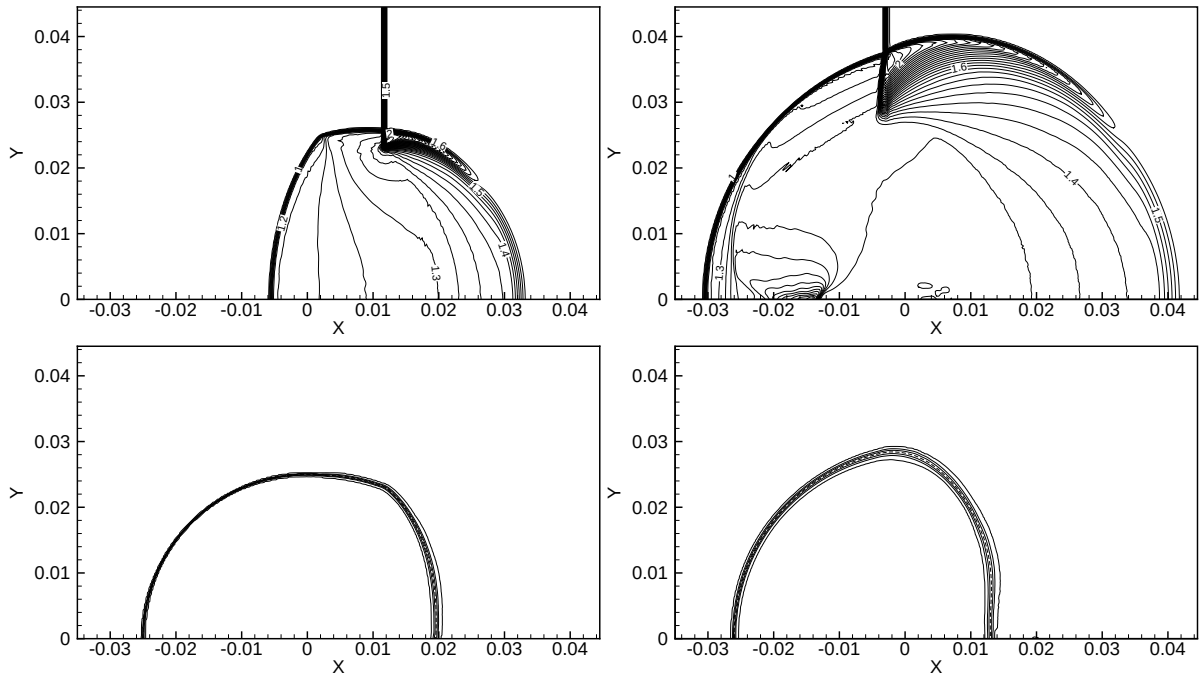

Figure 6.9: Shock hitting helium bubble, pressure (above) and volume fraction (below) at $t = 10.74 \times 10^{-3}$ and $t = 22.74 \times 10^{-3}$.

the speed of the refracted wave. The lower value for the experiment could mean that the equation of state, that is used for the helium–air mixture, is not very accurate. Also, the contamination in the experimental bubble is probably not uniform, but concentrated near the interface. Still, the agreement with the Quirk and Karni computation (that uses the same mixture EOS) is very good.

	c_s (m/s)		c_r (m/s)		u_{ri} (m/s)	
Present method	419	–	950	–	173	–
Quirk & Karni	422	(0.7)	943	(0.7)	178	(2.9)
Experiment	410	(2.1)	900	(5.3)	170	(1.7)

Table 6.5: Centerline wave speeds in helium bubble test: comparison of present method with computations by Quirk and Karni [23] and experiment by Haas and Sturtevant [11]. The difference with the present method in % is given in brackets. c_s: incident shock speed, c_r: shock speed in bubble, u_{ri}: right side of interface speed.

Chapter 7
Conclusion

7.1. Current work

A conservative surface-capturing method is developed for compressible two-fluid flow. The method is based on a physical model for numerical mixture flow. From this model, five flow equations are derived: three bulk-fluid equations and mass and energy equations for one of the pure fluids. It is also found, that pure-fluid equations of state can be used for the thermodynamic behaviour of the mixture flow.

A source term in the last, energy equation models the exchange of energy between the fluids. This exchange happens only through work: the fluids do not exchange heat. The source term can be integrated exactly through a shock wave, thus giving an exact closure for the system, in the case of discontinuous flow.

The numerical discretisation uses Linde's HLL approximate Riemann solver. This solver can be easily adapted to different flow equations and is therefore very useful for the two-fluid model. Simplified expressions for the wave speeds in Linde's solver appear to work well. The HLL solver can be used in combination with a second-order accurate limited flux discretisation. However, the choice of the limited variables has a large influence on the performance of the Riemann solver. It is found that the limiter has to be applied to primitive state variables for the best performance.

The energy exchange source term must be added to the Riemann solver and to the time integration of the solution. An approximate version of the source term greatly simplifies the computations this involves.

Results of 1D shock tube problems show that the method is indeed pressure-oscillation free: the solutions are continuous over the interface. Shock waves and interfaces are captured very well. Only for some very strong shocks, the approximate source term produces some small wiggles. These disappear on grid refinement.

Two shock-bubble interaction problems confirm that the method is easily extended to 2D. Shocks and interfaces are captured sharply and there are no pressure oscillations. Implementation of the method in an existing 2D code proved to be very simple.

7.2. Future research

The method described here works fine. However, possibilities for refinement exist, especially concerning the Riemann solver.

Godunov solver. The analytical expression for the source term in discontinuities can be used in Riemann solvers that are based on real, physical waves, like the exact Riemann solver of the Godunov scheme or a simplification of that solver.

Osher solver. With the Riemann invariants for the system known, it is possible to construct an Osher solver. The advantage of the Osher solver is that it is very accurate, yet does not contain shock waves, so the shock-version of the discontinuity source term is not even needed. However, the solver is expected to require numerical integration in determining the Riemann invariants.

HLL boundary conditions. It is worthwhile to study the possibility of applying more sophisticated boundary conditions to the HLL solver, that fit in with the integral approach of the HLL scheme and enforce the right number of conditions for each boundary. Possible boundary conditions are suggested by Van der Vegt and Van der Ven [32].

Multi-D upwinding. The resolution of curved contact discontinuities in the present method may be improved by using cell face state reconstructions that depend on the local direction of the flow.

Fluctuation splitting. A very good spatial discretisation of the current flow equations can probably be achieved with fluctuation splitting schemes [24]. They allow simultaneous and consistent treatment of the convective terms and the source terms, as well as multi-D upwinding [25].

References

1. R. Abgrall. How to prevent pressure oscillations in multicomponent flow calculations: A quasi conservative approach. *J. Comp. Phys.*, 125:150–160, 1996.
2. R. Abgrall and S. Karni. Computations of compressible multifluids. *J. Comp. Phys.*, 169:594–623, 2001.
3. R. Abgrall and R. Saurel. Discrete equations for physical and numerical compressible multiphase mixtures. *J. Comp. Phys.*, 186:361–396, 2003.
4. M. R. Baer and J. W. Nunziato. A two-phase mixture theory for the deflagration-to-detonation transition (DDT) in reactive granular materials. *Int. J. Multiphase Flows*, 12:861–889, 1986.
5. P. Batten, N. Clarke, C. Lambert, and D. M. Causon. On the choice of wavespeeds for the HLLC Riemann solver. *SIAM J. Sci. Comput.*, 18(6):1553–1570, 1997.
6. E. H. v. Brummelen and B. Koren. A pressure-invariant conservative Godunov-type method for barotropic two-fluid flows. *J. Comp. Phys.*, 185:289–308, 2003.
7. R. Courant and K. O. Friedrichs. *Supersonic Flow and Shock Waves*. Springer Verlag, New York, 1976.
8. G. F. Duivesteijn. Improved capturing of contact discontinuities for two-fluid flows. Note MAS-N0202, CWI, Centre for Mathematics and Computer Science, Amsterdam, Dec. 2002.
9. R. P. Fedkiw, T. Aslam, B. Merriman, and S. Osher. A non-oscillatory Eulerian approach to interfaces in multimaterial flows (the Ghost Fluid Method). *J. Comp. Phys.*, 152:457–492, 1997.
10. H. Guillard and A. Murrone. A five-equation reduced model for compressible two phase flow problems. INRIA Rapport de recherche N^o 4778, Institut National de Recherche en Informatique et en Automatique, Sophia Antipolis, Mar. 2003.
11. J. F. Haas and B. Sturtevant. Interaction of weak shock waves with cylindrical and spherical gas inhomogeneities. *J. Fluid Mech.*, 81:41–76, 1987.
12. A. Harten, P. D. Lax, and B. v. Leer. On upstream differencing and Godunov-type schemes for hyperbolic conservation laws. *SIAM Review*, 25(1):35–61, 1983.
13. C. W. Hirt and B. D. Nichols. Volume of fluid (VOF) method for the dynamics of free boundaries. *J. Comp. Phys.*, 39:201–225, 1981.
14. A. K. Kapila, R. Menikoff, J. B. Bdzil, S. F. Son, and D. S. Stewart. Two-phase modeling of deflagration-to-detonation transition in granular materials: Reduced equations. *Physics of Fluids*, 13(10):3002–3024, 2001.
15. S. Karni. Multicomponent flow calculations by a consistent primitive algorithm. *J. Comp. Phys.*, 112:31–43, 1994.
16. B. Koren. A robust upwind discretization method for advection, diffusion and source terms. In C. B. Vreugdenhil and B. Koren, editors, *Numerical Methods for Advection-Diffusion Problems*, volume 45 of *Notes on Numerical Fluid Mechanics*, pages 117–138, Braunschweig, 1993. Vieweg.
17. B. Koren, M. R. Lewis, E. H. v. Brummelen, and B. v. Leer. Riemann-problem and level-set approaches for homentropic two-fluid flow computations. *J. Comp. Phys.*, 181:654–674, 2002.
18. B. v. Leer. Upwind-difference methods for aerodynamic problems governed by the Euler equations. In *Lectures in Applied Mathematics*, volume 22, part 2, pages 327–336, Providence, RI, 1985. American Mathematical Society.
19. T. Linde. A practical, general-purpose, two-state HLL Riemann solver for hyperbolic conservation laws.

Int. J. Numer. Meth. Fluids, 40:391–402, 2002.

20. A. Marquina and P. Mulet. A flux split algorithm applied to conservative models for multicomponent compressible flows. *J. Comp. Phys.*, 185:120–138, 2003.
21. S. P. Marsh. *LASL Shock Hugoniot Data*. Univ. of California Press, Berkeley, 1980.
22. W. Mulder, S. Osher, and J. A. Sethian. Computing interface motion in compressible gas dynamics. *J. Comp. Phys.*, 100:209–228, 1992.
23. J. J. Quirk and S. Karni. On the dynamics of a shock-bubble interaction. ICASE Report 94-75, Institute for Computer Applications in Science and Engineering, NASA Langley Research Center, Hampton, VA, Sept. 1994.
24. P. L. Roe. Fluctuations and signals, a framework for numerical evolution problems. In K. W. Morton and M. J. Baines, editors, *Numerical Methods for Fluid Dynamics*, pages 219–257. Academic Press, 1982.
25. P. L. Roe. Linear advection schemes on triangular meshes. CoA Report 8720, Cranfield Institute of Technology, Cranfield, Bedford, Nov. 1987.
26. R. Saurel and R. Abgrall. A multiphase Godunov method for compressible multifluid and multiphase flows. *J. Comp. Phys.*, 150:425–467, 1999.
27. H. J. Schroll and F. Svensson. A bi-hyperbolic finite volume method on quadrilateral meshes. preprint, Centre for Mathematical Sciences, Lund University, Lund, Apr. 2004.
28. M. Sussman, P. Smereka, and S. Osher. A level set approach for computing solutions to incompressible two-phase flow. *J. Comp. Phys.*, 114:146–159, 1994.
29. P. K. Sweby. High resolution schemes using flux limiters for hyperbolic conservation laws. *SIAM J. Num. Anal.*, 21:995–1011, 1984.
30. V. T. Ton. Improved shock-capturing methods for multicomponent and reacting flows. *J. Comp. Phys.*, 128:237–253, 1996.
31. E. F. Toro. *Riemann Solvers and Numerical Methods for Fluid Dynamics*. Springer-Verlag, Berlin, 1997.
32. J. J. W. v. d. Vegt and H. v. d. Ven. Slip flow boundary conditions in discontinuous Galerkin discretizations of the Euler equations of gas dynamics. In *Fifth World Congress on Computational Mechanics*, Vienna, Austria, 2002.
33. J. Wackers. An adaptive-gridding solution method for the 2D unsteady Euler equations. Note MAS-N0301, CWI, Centre for Mathematics and Computer Science, Amsterdam, Jan. 2003.
34. J. Wackers and B. Koren. A simple and efficient space-time adaptive grid technique for unsteady compressible flows. AIAA Paper 2003-3825, American Institute of Aeronautics and Astronautics, July 2003.

Appendix I
Approximate model for mixture-fluid shocks

"It is striped, what about ze panties? (5)"[1]

The relations given for mixed-fluid shocks in section 3.3 are rather involved. Earlier in the current project, an approximate model was derived for shocks running into two-fluid mixtures with a constant state. It is included here for completeness. The difference with the model from chapters 2 and 3 is, that the current model is meant to compute shocks in physical mixtures, that can have different pressures in the two fluids. The other model is primarily aimed at modeling the interface region, where the mixture is supposed to behave like a single fluid.

I.1. THE 'ZEBRA' MODEL

We consider a shock, running into a mixture as described in section 2.1. The state of the mixture is constant in the entire pre-shock region and it is a real mixture ($0 < \alpha < 1$). The shock consists of many small shocks in the pure-fluid elements, running with the local pure-fluid shock speed (which is well defined) and a complex pattern of adaptation waves appears behind the shocks, to make the pressure and velocity of all elements equal. This leveling-out is called 'relaxation'. The sum of all these waves appears as one shock wave. Examples of the adaptation waves can be found in Saurel and Abgrall [26] and Quirk and Karni [23], for a bubble.

The wave pattern described above is too difficult to model exactly. Therefore, we compute a shock speed for a simplified distribution of the two fluids. The simplest distribution is that of a shock tube with the fluids in two layers, one fluid above and the other below, with the shock running simultaneously into both of them. Unfortunately, this model is wrong, as a slow shock could run *slower* than the sound speed in the material with the highest sound speed. This is clearly impossible.

A much better model is the 'zebra' model: the shock tube is filled with many thin discs of the two fluids in a row and the shock runs alternately in fluid 1 and 2. The mixture-fluid shock speed is then simply the average travel speed of the shock. This average is found by considering two discs, one of each fluid, with a total length l (see figure I.1). The time it takes for the shock to cross this length is:

$$\tau = \frac{\alpha l}{c_{s_1}} + \frac{(1-\alpha)l}{c_{s_2}},$$

with c_{s_1} and c_{s_2} the pure-fluid shock speeds. Therefore, the average shock speed is:

$$c_s = \frac{l}{\tau} = \frac{1}{\frac{\alpha}{c_{s_1}} + \frac{1-\alpha}{c_{s_2}}}. \tag{I.1}$$

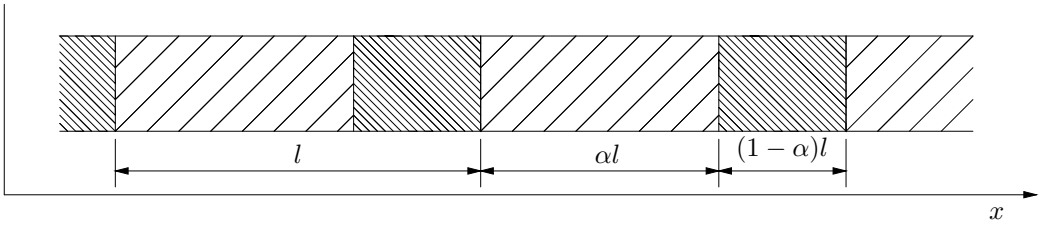

Figure I.1: 'Zebra' fluid distribution.

[1] Colin Dexter, *The Way Through the Woods*, quoting from a crossword puzzle.

We need a compatibility condition that relates the shock speeds c_{s_1} and c_{s_2} in the pure fluids to each other. The condition that makes most sense is that the fluid velocities behind the shock are equal. In reality, the velocities and pressures are probably both unequal and they relax after the shock has passed. Pressure relaxation can happen by compression and expansion in the up-down direction and we can imagine that the same happens in the zebra model, with some bypass between the fluids. But if the fluids have different velocities, then adaptation waves appear that travel backward, each time the shock crosses an interface. However, a shock moving through a nicely mixed two-fluid medium does not create backward-moving waves. The only way to eliminate those waves is to make the velocities of the fluids equal.

All that is needed now, is an expression for the shock speeds in pure fluids, which is readily found from the single-fluid Rankine-Hugoniot relations. If the gas satisfies the ideal-gas EOS (2.8), then the pure-fluid shock speed for a shock moving into a gas at rest ($u = 0$) is:

$$c_s = \frac{\gamma+1}{4}[u] + \sqrt{\left(\frac{\gamma+1}{4}[u]\right)^2 + \gamma\frac{p_{pre}}{\rho_{pre}}}. \tag{I.2}$$

This expression is combined with equation (I.1):

$$c_s = \frac{1}{\frac{\alpha}{\frac{\gamma_1+1}{4}[u]+\sqrt{\left(\frac{\gamma_1+1}{4}[u]\right)^2+\gamma_1\frac{p_{pre}}{\rho_{1,\,pre}}}} + \frac{1-\alpha}{\frac{\gamma_2+1}{4}[u]+\sqrt{\left(\frac{\gamma_2+1}{4}[u]\right)^2+\gamma_2\frac{p_{pre}}{\rho_{2,\,pre}}}}}. \tag{I.3}$$

This equation relates the shock speed and the velocity change for a shock running into a mixture ideal fluid at rest.

I.2. Alloy test

Experimental data for shocks in mixtures as described above are difficult to obtain, because that kind of mixture does not often appear in nature. One example are metal alloys. Two mixed metals do not really blend up to atom level, but one metal forms small elements in the other. The alloy can thus be seen as a two-fluid mixture and for strong shocks, it behaves like a compressible fluid. Furthermore, shock speed data for alloys are available, e.g., from Marsh [21], so they can be used to test the shock-speed relations given above (Saurel and Abgrall [26] use this test for their numerical method).

Three alloys are studied here, uranium / rhodium, epoxy / spinel (not a metal alloy, probably spinel powder in epoxy) and gold / germanium. Properties of these alloys are given in table I.1. The equation of state which is used for the pure fluids is the stiffened-gas equation of state,

$$p = (\gamma-1)\rho e - \gamma\pi. \tag{I.4}$$

For this equation, the stiff-gas parameters γ and π for the pure fluids are needed. These are determined experimentally and given in table I.2.

Alloy	α	ρ (kg/m^3)
Uranium / Rhodium	0.809	17204
Epoxy / Spinel	0.600	2171
Gold / Germanium	0.730	15536

Table I.1: Material properties for three alloys (from Marsh [21]). α refers to the first material.

For the stiffened-gas EOS, the pure-fluid shock-speed relation is

$$c_s = \frac{\gamma+1}{4}[u] + \sqrt{\left(\frac{\gamma+1}{4}[u]\right)^2 + \gamma\frac{p_{pre}+\pi}{\rho_{pre}}}, \tag{I.5}$$

Material	ρ (kg/m^3)	c (m/s)	γ	π (GPa)
Uranium	18930	2510	3.52	33.9
Rhodium	12492	4790	3.61	79.0
Epoxy	1185	2823	2.45	5.6
Spinel	3622	7954	1.50	157.1
Gold	19204	3250	3.57	15.6
Germanium	5328	?	2.92	12.5

Table I.2: Stiff-gas parameters for the six pure materials (from Marsh [21]).

so the mixture shock speed becomes

$$c_s = \frac{1}{\frac{\alpha}{\frac{\gamma_1+1}{4}[u]+\sqrt{\left(\frac{\gamma_1+1}{4}[u]\right)^2+\gamma_1\frac{p_{pre}+\pi_1}{\rho_{1,\,pre}}}} + \frac{1-\alpha}{\frac{\gamma_2+1}{4}[u]+\sqrt{\left(\frac{\gamma_2+1}{4}[u]\right)^2+\gamma_2\frac{p_{pre}+\pi_2}{\rho_{2,\,pre}}}}}. \tag{I.6}$$

The results from this equation can be compared with measurements of the relation between shock speed and material speed for the alloys. The tests are done with the alloys in initial conditions as given in table I.1, with an initial pressure $p = 10^5$ Pa and velocity zero. Results are given in figure I.2. Curves are plotted for the pure fluids (equation (I.5)) and for the mixture fluid (equation (I.6)). The mixture curve is compared with experimental data.

We see that equation (I.6) gives an excellent fit to the experimental data for the first two alloys. The prediction of the uranium-rhodium shock speed is good over the entire speed range, even though the alloy does not consist of pure-fluid elements. Instead, uranium and rhodium can dissolve a bit in each other, so the elements consist of uranium with a little rhodium and rhodium with a little uranium. This does not appear to influence the shock-speed prediction. The epoxy-spinel shock speed is especially good for strong shocks. This is not caused by the mixture-fluid model but by the stiffened-gas EOS, which gives an inaccurate prediction of the epoxy shock speed for weak shocks. If the stiffened-gas parameters are tuned to give the correct shock speeds for weak shocks, then the mixture-model performs much better for these shocks.

A caveat: the model does not work for all alloys. Gold-germanium is a particularly striking example. There, the mixture shock speed does not even lie in between the pure-fluid speeds, so the shock speed prediction is obviously wrong. Apparently, this alloy has some physical properties that do not agree with the zebra model.

Concluding: the model suggested in the previous section appears to be a reasonable approximation of the behaviour of shocks in most alloys. If used with care, it can be very useful for alloy simulation.

a)

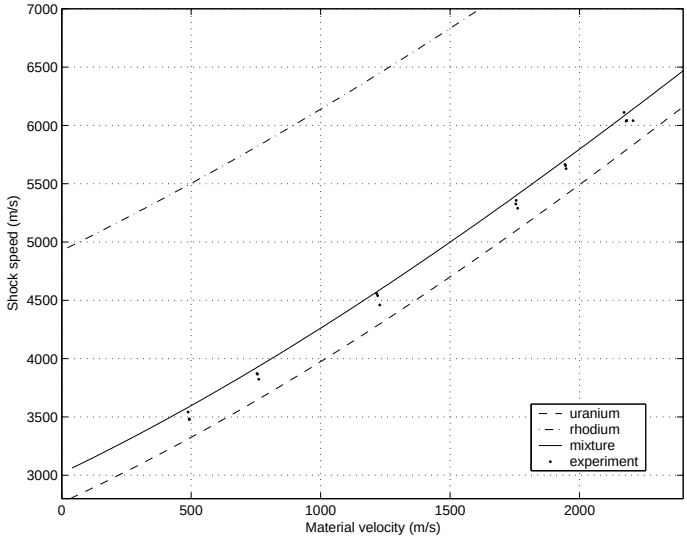

b)

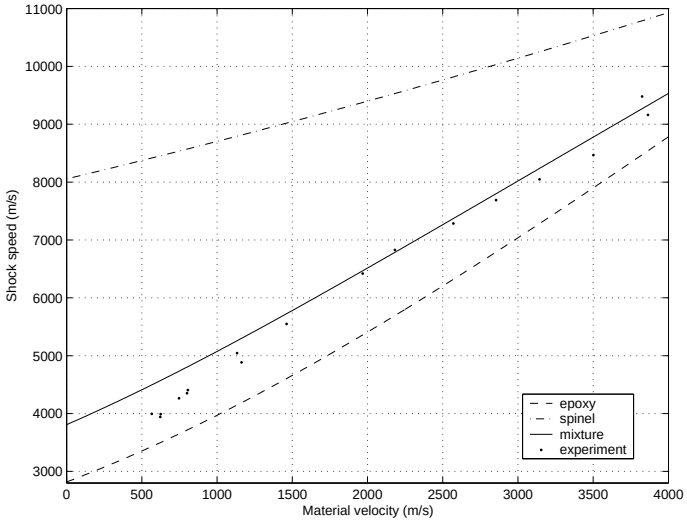

c)

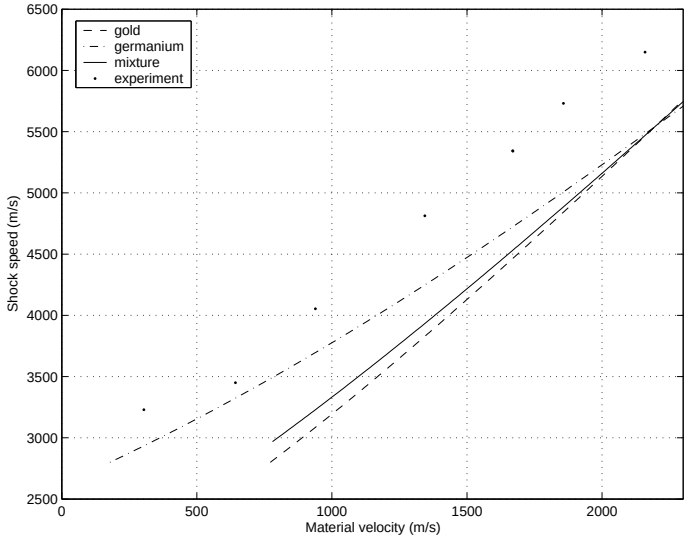

Figure I.2: Shock speed versus material velocity for three alloys.

Appendix II
Oblique shock–interface interaction

In the initial phase, the shock–bubble interaction problems from section 6.2 show an interaction that is a very local phenomenon. It takes place at one point only: the point where the incoming shock hits the interface. Because the interaction is local and does not (yet) depend on the flow in the rest of the domain, it is equivalent to the problem of a shock hitting an oblique plane interface. This problem can be solved analytically.

In this appendix, we study the interaction of the shock from the bubble problem, with plane air–helium and air–R22 interfaces. The results are compared with the shock–bubble interactions and are used to interpret the phenomena that appear in the shock–bubble problems.

II.1. Problem setup

Consider a problem as in figure II.1a, a vertical shock impacting on an inclined two-fluid interface. Both the shock and the interface have an infinite length, so the shape of the solution does not change in time. It is convenient to use a coordinate system that is attached to the point of impact of the shock, as the flow is steady in that coordinate system (see figure II.1b). The figure shows the incoming shock s, running into region I and impacting on the interface. Two waves originate from the impact point: the refracted shock running into the undisturbed fluid below the interface and the adaptation wave a running into the region II behind the incoming shock.

The flow in the region II can be determined from geometrical considerations only, this is done in the current section. The flow in the region III and the waves r and a depend on the aerodynamic properties of the two fluids, they are different for different fluids on both sides of the interface. The following two sections treat this part of the flow for the specific air–helium and air–R22 cases considered. When examples are given, the initial conditions are always those of the shock–bubble problems from section 6.2: the incoming shock has a Mach number $M_s = 1.22$ and the gas states are as given in table 6.3.

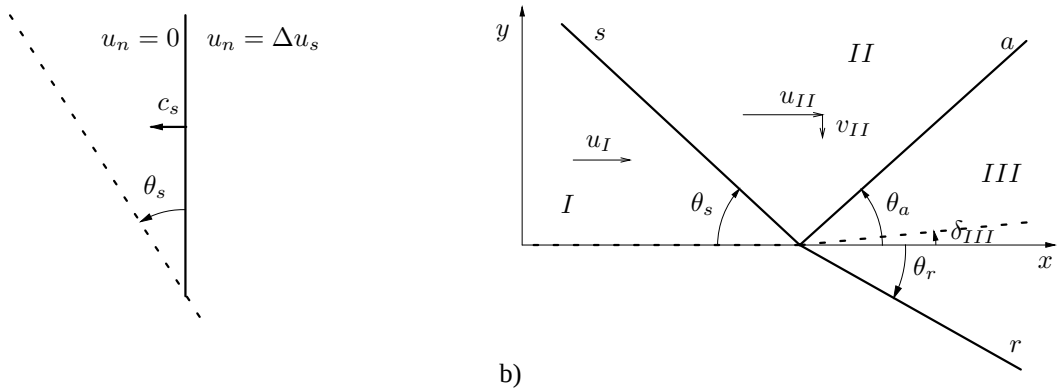

Figure II.1: Shock hitting an oblique interface (a) and transformation of this flow into shock-fixed coordinates (b).

In front of the shock, the region I is divided in two by the interface. This region has a pressure p_I, the density is $\rho_{1,I}$ above the interface and $\rho_{2,I}$ below. The velocity is:

$$u_I = c_s / \sin\theta_s. \tag{II.1}$$

As both parts of region I have equal velocities and constant sound speeds, the ratio of the Mach numbers above and below the interface is constant:

$$\begin{aligned} M_{1,I} &= \frac{u_I}{\sqrt{\gamma_1 p_I/\rho_{1,I}}}, \\ M_{2,I} &= \frac{u_I}{\sqrt{\gamma_2 p_I/\rho_{2,I}}} = M_{1,I}\sqrt{\frac{\gamma_1}{\gamma_2}\frac{\rho_{2,I}}{\rho_{1,I}}}. \end{aligned} \tag{II.2}$$

We see, from equation (II.1), that the Mach numbers decrease from ∞ as θ_s increases. For $\theta_s = 90^o$, the Mach number $M_{1,I}$ is equal to the Mach number of the normal shock $M_s = c_s/\sqrt{\gamma_1 p_I/\rho_{1,I}}$.

The region II lies behind the incoming shock s. Note that, whatever the value of θ_s is, this is always *the same shock*, so the pressure p_{II} and density ρ_{II} do not change with θ_s. They are always found with the relations for normal shocks, using a shock speed c_s and a velocity jump Δu_s. So the velocity components in II are:

$$\begin{aligned} u_{II} &= c_s/\sin\theta_s - \Delta u_s \sin\theta_s, \\ v_{II} &= \Delta u_s \cos\theta_s. \end{aligned} \tag{II.3}$$

The flow angle δ_{II} is:

$$\delta_{II} = \arctan\frac{v_{II}}{u_{II}}. \tag{II.4}$$

This function is plotted in figure II.2a, for $M_s = 1.22$ (the Mach number for the shock-bubble tests). It is seen from this figure that δ_{II} has a maximum, somewhere between $\theta_s = 0^o$ and $\theta_s = 90^o$. Another important transition occurs for some θ_s above the θ for maximum deflection: the Mach number M_{II} behind the shock,

$$M_{II} = \frac{\sqrt{u_{II}^2 + v_{II}^2}}{\sqrt{\gamma_1 p_{II}/\rho_{II}}}, \tag{II.5}$$

drops below 1 (see figure II.2b). For higher θ_s, the flow behind shock s is subsonic.

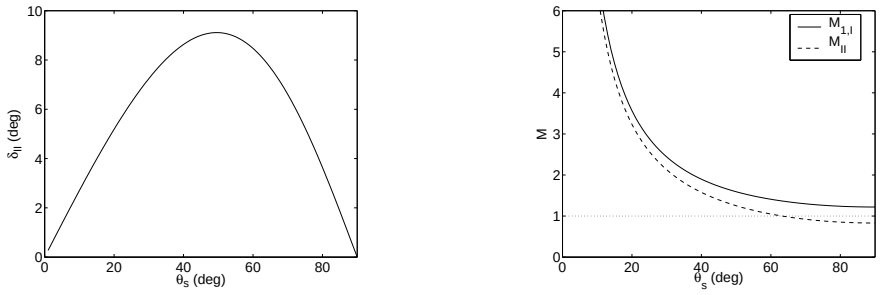

Figure II.2: Flow angle behind the incoming shock (a) and Mach number before / behind the incoming shock (b). Normal-shock Mach number $M_s = 1.22$.

When the shock hits the two-fluid interface, it continues in fluid 2 as the refracted shock r. An adaptation wave a runs back into fluid 1. The refracted wave r is always a shock, a can be either a shock or an expansion fan. Their strengths are such, that the pressures and the flow angles behind the waves are equal. Both wave strengths depend on the angle θ_s and on the properties of the two gases. The computation of the wave properties can be found in any text book on gas dynamics, see e.g. [7]. It is not treated in detail here.

When θ_s is increased, a point appears where the flow pattern as in figure II.1 breaks up. Both the type of this break-up and the type of the adaptation wave a for smaller values of θ_s depend on the ratio of the Mach numbers in the unperturbed flow in I. Two cases are possible: $M_{1,I} > M_{2,I}$ or $M_{2,I} > M_{1,I}$. The air–helium and air–R22 interfaces are examples of these two cases. They are treated separately below.

II.2. AIR – REFRIGERANT R22

When the fluid below the interface has a high density, then its sound speed is low, so the resulting Mach number $M_{2,I}$ is high: $M_{2,I} > M_{1,I}$. In the simulation of the air–R22 bubble problem in section 6.2, we saw that the shock wave in the dense R22 runs slower than in air.

The state III and the strength of the waves r and a are found by writing expressions for the two waves, given the pre-conditions $I, 2$ and II and some post-pressure p_{III}, which is the same for both fluids. Then p_{III} is varied until a value is found for which the δ's of the fluids are equal too. This will be done numerically.

The shape of the shock–interface interaction and the type of the adaptation wave a can already be seen from figure II.3. This (general) figure gives the flow turning angle δ for an oblique shock, as a function of the initial Mach number and of the pressure ratio across the shock, for air. We shall use it to compare the shocks s and r. The different values of δ_{II}, the turning angle behind s, are easily found in this figure: the pressure jump across wave s is constant, so all the states II for $0^o \leq \theta_s \leq 90^o$ lie on a straight line of constant pressure, which is dotted in figure II.3.

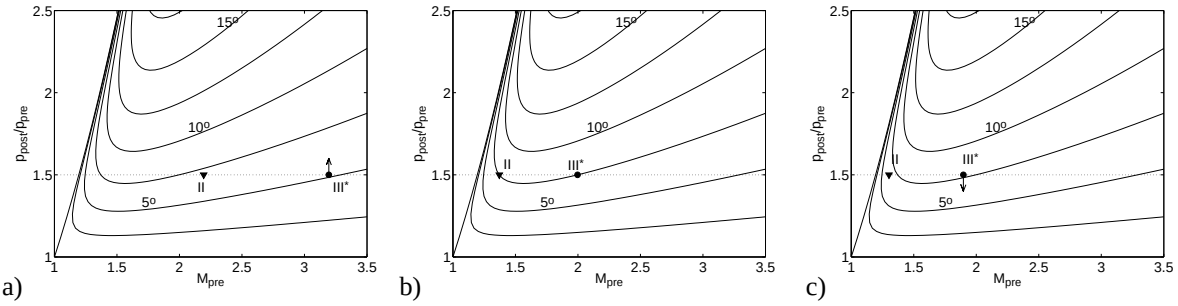

Figure II.3: An example diagram of the flow angle δ for an oblique shock in air, depending on the pre-shock Mach number and the pressure ratio over the shock. The symbol ▼ denotes the shock s, the symbol • the shock that appears when fluid $2, I$ is brought to p_{II}. This diagram applies when $M_{2,I} > M_{1,I}$.

Now we can find the type of the adaptation wave a by looking at r, especially at what happens if r brings fluid 2 to the same pressure as s does to fluid 1. Figure II.3a gives an example for a low θ_s. (For simplicity, the fluid 2 is supposed to be air too, so the same curves are valid for fluids 1 and 2. But for air and R22, the principle is the same.) We know that $M_{2,I}$ is larger than $M_{1,I}$. So if the fluid 2 were compressed to the pressure p_{II}, then its deflection δ^*_{III} would be less than δ_{II} (see figure II.3a). Therefore, the fluid 2 is compressed more than that: the actual angle δ_{III} is higher than δ^*_{III} and the pressure p_{III} is higher than p_{II}. Fluid 1 must get this same, higher pressure, which means that a must be an oblique shock wave. This is nice, as a shock wave deflects the fluid 1 back upwards, which reduces the required deflection angle for fluid 2. Thus, the fluids 1 and 2 are adapted to each other in the domain III.

However, we see that δ_{II} has a maximum somewhere on the dotted line. So as $M_{1,I}$ decreases below the Mach number for that maximum, we find a point somewhere, where δ_{II} and δ^*_{III} are the same (figure II.3b). The oblique shocks in fluid 1 and 2 are different, but they deflect the fluids to the same angle at the same pressure. In that case, no adaptation wave is needed in fluid 1, so wave a vanishes. For even lower $M_{1,I}$, the angle δ^*_{III} is higher than δ_{II}, so the fluid 2 is compressed to a lower pressure than p_{II}, reducing δ_{III} (figure II.3c). Then the adaptation wave a is an expansion! This wave deflects the fluid 1 further than δ_{II}, so, again, the pressures and deflection angles are matched.

So the character of the adaptation wave is not constant: as θ_s is increased, the adaptation wave changes from a shock into an expansion fan somewhere.

Another important phenomenon is the breakdown of the flow pattern. For high θ_s, the flow as in figure II.1 cannot exist anymore. Instead, a more complex wave system appears that has some length scale and is thus not local anymore. Let us study what happens when θ_s increases. For a heavy fluid 2, the breakdown always starts

in fluid 1, but the cause of the breakdown differs. If the adaptation wave is an expansion fan, the breakdown starts when M_{II} drops below 1 (see figure II.2). In the resulting subsonic flow, an expansion wave is no longer possible, so the flow pattern breaks up. In this case, the angle θ_s for breakdown does not depend on the fluid 2, as M_{II} depends only on θ_s.

On the other hand, if the breakdown occurs when a is still a shock wave, then it has another cause. It can be seen from figure II.3 that at each Mach number M_1, the flow has a maximum possible δ, occurring for some pressure ratio. This maximum deflection decreases to zero as M_1 approaches 1. So when M_{II} comes close to 1, a moment appears where the wave a is unable to create a δ that is big enough to match fluid 1 to fluid 2. This happens when M_{II} is still *larger* than 1.

But whatever the cause, the result of the breakdown is the same: the adaptation wave cannot remain attached to the point where the shock hits the two-fluid interface. Its starting point 'climbs' up the incoming shock wave and it gets a curved shape. This phenomenon can be clearly seen in the bubble simulation, figure 6.5.

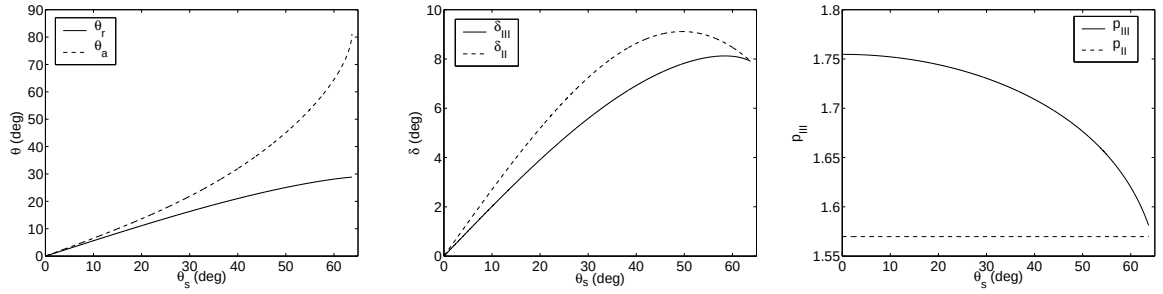

Figure II.4: Oblique shock hitting air–R22 interface: shock angles, flow angles and post-shock pressures as functions of the incoming shock angle θ_s. The figures end on flow breakdown.

Let us now study the air–R22 case (figure II.4), with flow parameters as in section 6.2. As M_{II} is lower than $M_{2,I}$, it is not surprising that we find $\theta_a > \theta_r$. Also, δ_{III} is smaller than δ_{II}, which corresponds to a shock wave a. The pressure p_{III} starts high, but decreases with increasing θ_s, which means that r and a become weaker. Flow breakdown starts just before the adaptation wave would vanish. (This is accidental: if the R22 density is lowered from 4.4 to 4.0, then the breakdown occurs when a has become an expansion). The Mach number M_{II} at breakdown is 1.0033, indeed more (though not much more) than 1.

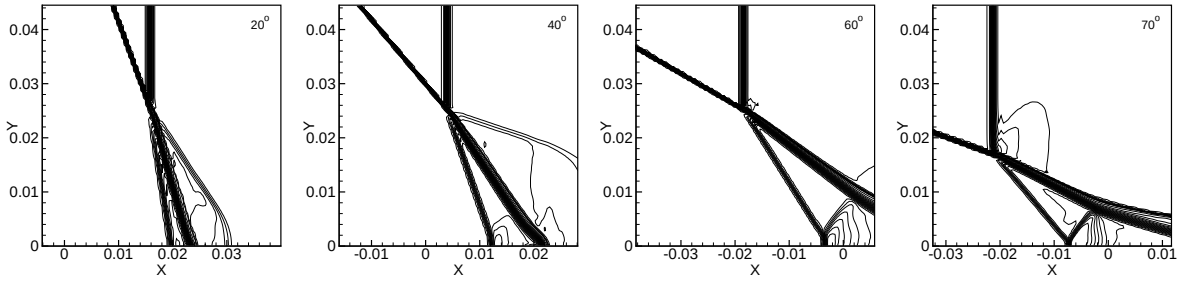

Figure II.5: Shock wave hitting a plane, oblique air–R22 interface: density profiles. The conditions are the same as for the bubble experiments in section 6.2, the grid has 100×200 cells.

Figure II.5 shows some actual simulations of a shock hitting a plane air–R22 interface. The shock strength and the simulation settings are the same as in the bubble simulations. As the impact angle θ_s increases, the adaptation wave becomes weaker until it has all but vanished at $\theta_s = 60^{\text{o}}$. At $\theta_s = 70^{\text{o}}$, we recognize the first part of a curved shock wave, behind the incoming shock and above the interface. This corresponds well with

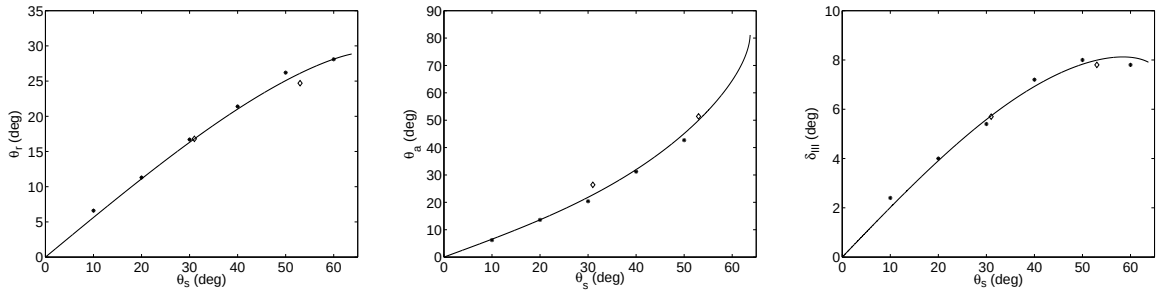

Figure II.6: Shock hitting air–R22 interface: comparison of analytic results from figure II.4 with plane-interface simulations ($*$, see figure II.5) and the shock–bubble simulation ($\diamond$).

the analytical breakdown angle of 64^{o} from figure II.4. The reflection of the refracted shock r on the lower, wall boundary is not relevant here, it does not influence the first interaction. Figure II.6 shows that these simulations correspond very well with the theory described above, especially considering the measurement error of about 1^{o} in the simulation angles. Also, the correspondence to the angles measured in the bubble simulation is good.

So in the air–R22 case, the local flat interface approximation is useful to study the phenomenology and the qualitative behaviour of the shock–bubble interaction.

II.3. Air – helium

When the fluid below the interface is lighter than above the interface, then it has a higher sound speed, so the Mach number $M_{2,I}$ is lower than $M_{1,I}$. We see in the bubble simulation, depicted in figure 6.8, that shock waves in helium run faster than in air.

The type of the adaptation wave is exactly the opposite of the previous case (see figure II.7): for low θ_s, the δ^*_{III} is higher than δ_{II}, so δ_{III} is lower than δ^*_{III} and the adaptation wave a is an expansion. Again, we find one Mach number where no adaptation wave is needed. For higher θ_s, the δ^*_{III} is too low, so a is a shock wave.

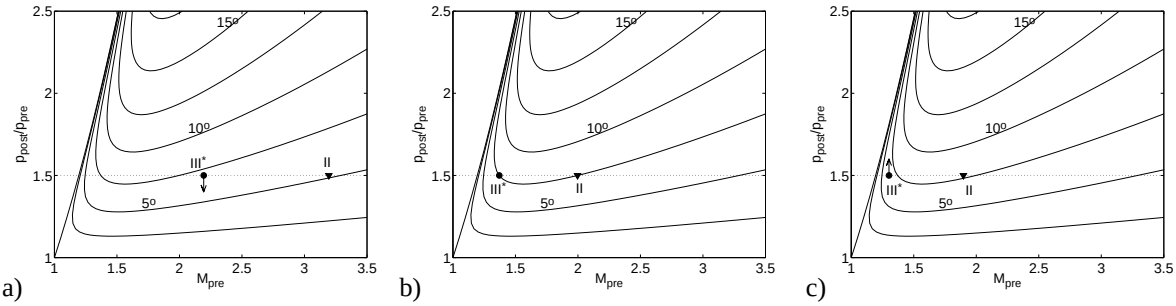

Figure II.7: An example diagram as in figure II.3, but now for $M_{2,I} < M_{1,I}$.

The breakup phenomenon for $M_{2,I} < M_{1,I}$ is totally different from the previous case. As $M_{2,I}$ is the lower Mach number, the breakup happens below the interface. The refracted wave r is always a shock wave, so the breakup is always initiated like the second type of breakup in the previous case: it starts when $M_{2,I}$ is so low that r is no longer able to produce the required δ_{III} to match fluid 2 to fluid 1. Consequently, the breakup occurs always at $M_{2,I} > 1$. When breakdown starts, the shock r moves forward. But in this case, it does not meet the incoming shock s, so it runs ahead of the point where s reaches the interface. Where the curved shock r hits the interface, an oblique shock is created in fluid 1, which runs backward until it crosses the incoming shock s. There, a complex λ-shock pattern is formed. The wave pattern can be seen very well in the bubble simulation, figure 6.8.

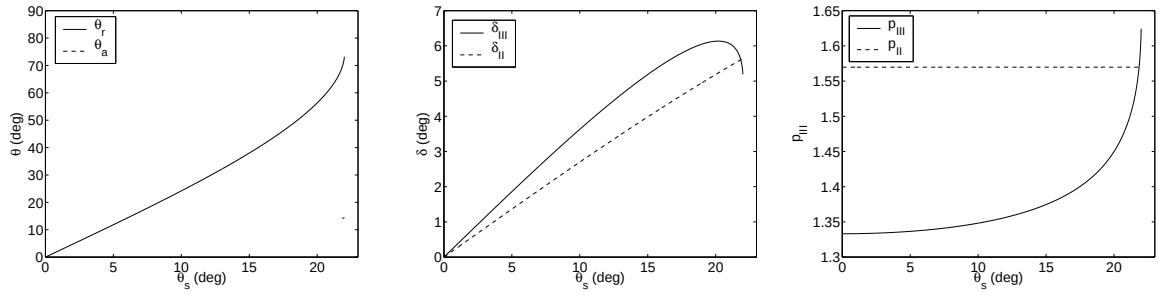

Figure II.8: Oblique shock hitting air–helium interface: shock angles, flow angles and post-shock pressures.

Looking at the actual air–helium case (figure II.8), we see indeed an initial expansion: the pressure p_{III} is lower than p_{II} and δ_{III} is higher than δ_{II}. But a changes to a shock, less than a degree below breakdown. Note the small line that indicates θ_a for this shock, in the first picture of figure II.8. Breakdown occurs at $\theta_s = 22.4^{\mathrm{o}}$.

Results from plane-interface simulations (figure II.9) show two things. First, the breakup happens indeed between $\theta_s = 20^{\mathrm{o}}$ and $\theta_s = 25^{\mathrm{o}}$, but it does not change the flow much. At $\theta_s = 25^{\mathrm{o}}$, an oblique shock above the interface starts from the curved refracted shock, but this shock is quickly absorbed by the expansion fan behind it. Only at a very high angle ($\theta_s = 40^{\mathrm{o}}$) do we see two really distinct waves behind each other.

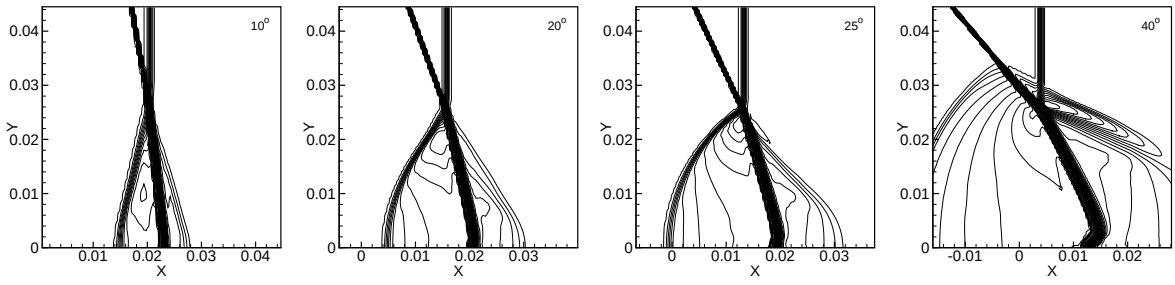

Figure II.9: Shock wave hitting a plane, oblique air–helium interface: density profiles.

And second: in this case, the wall at $y = 0$ does influence the shock–interface interaction above it. The refracted wave is curved, meeting the lower (wall) boundary at right angles. This curvature has some effect on the density distribution near the impact point. So the phenomenon is not strictly local anymore and, in principle, the analysis given above does not apply. In spite of this, the correspondence between the experiments and the analysis is quite good (see figure II.10). But also in the bubble case (figure 6.8) the interaction is not strictly local. And the angles measured here differ significantly from the analysis: the effect of the curved interface is to lower the deflection angle δ_{III} and to postpone the breakup to $\theta_s \approx 30^{\mathrm{o}}$. At this angle, the oblique shock above the interface is hardly noticeable, even less than in the plane-interface case.

So concluding, the local plane-interface approximation gives the qualitative behaviour of the air–helium shock–bubble interaction correctly. But the interaction is influenced by the curved interface so, quantitatively, it is not predicted accurately by the analysis.

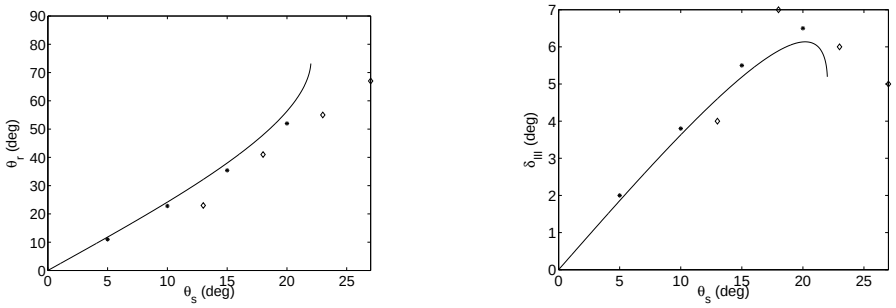

Figure II.10: Shock hitting air–helium interface: comparison of analytic results from figure II.8 with plane-interface simulations ($*$, see figure II.9) and the shock–bubble simulation ($\diamond$).